

**Decreasing trends of ammonia emissions over Europe seen
from remote sensing and inverse modelling**

**Ondřej Tichý¹, Sabine Eckhardt², Yves Balkanski³, Didier Hauglustaine³,
Nikolaos Evangeliou^{2,*}**

¹ The Czech Academy of Sciences, Institute of Information Theory and Automation, Prague,
Czech Republic.

² Norwegian Institute for Air Research (NILU), Department of Atmospheric and Climate
Research (ATMOS), Kjeller, Norway.

³ Laboratoire des Sciences du Climat et de l'Environnement (LSCE), CEA-CNRS-UVSQ,
91191, Gif-sur-Yvette, France.

* Corresponding author: N. Evangeliou (Nikolaos.Evangeliou@nilu.no)

Abstract

Ammonia (NH₃), a significant precursor of particulate matter, **not only** affects biodiversity, ecosystems, soil acidification, **but also** climate and human health. In addition, its concentrations are constantly rising **due to** increasing feeding needs **and the** large use of **fertilization** and animal farming. **Despite the** significance of ammonia, its emissions are associated with large uncertainties, while its atmospheric abundance is difficult to measure. **Nowadays**, satellite products **can** effectively **measure ammonia**, with low uncertainty, and a global coverage. Here, we use satellite observations of column ammonia in combination with an inversion algorithm to derive ammonia emissions with a high resolution over Europe for the period 2013–2020. Ammonia emissions peak in Northern Europe, due to agricultural application and livestock management, **in** Western Europe (industrial activity) and over Spain (pig farming). Emissions have decreased by -26% since 2013 (from 5431 Gg in 2013 to 3994 Gg in 2020) showing that the abatement strategies adopted by the European Union have been very efficient. The slight increase (+4.4%) **in** 2015 is also reproduced here and is attributed to some European countries exceeding annual emission targets. Ammonia emissions are low in winter (286 Gg) and peak in summer (563 Gg) and are dominated by the temperature dependent volatilization of ammonia from the soil. The largest emission decreases were observed in Central and Eastern Europe (-38%) and in Western Europe (-37%), while smaller decreases were recorded in Northern (-17%) and Southern Europe (-7.6%). **When** complemented against ground observations, modelled concentrations using the posterior emissions showed improved statistics, also following the observed seasonal trends. The posterior emissions presented here also agree well with respective estimates reported in the literature and inferred from **bottom-up** and **top-down** methodologies. These results indicate that satellite measurements **combined with inverse algorithms** constitute a robust **tool for emission** estimates and **can infer the** evolution of ammonia emissions **over large timescales**.

Deleted: is the most important alkaline gas in the atmosphere and directly ...

Deleted: . It also indirectly affects

Deleted: because of the

Deleted: of the global population accompanied by a

Deleted: r

Deleted: fertilizers

Deleted: The combination of its increasing atmospheric levels with its environmental and human impact has led many countries to adopt abatement strategies in order to conform with respective regulations. While the...

Deleted: is pronounced,

Deleted: often

Deleted: However, during the last decade, several

Deleted: have been developed that measure ammonia very

Deleted: ,

Deleted: ,

Deleted: most importantly, with

Deleted: ¶

Deleted: and the local maxima are found over

Deleted: Our calculations show that these e

Deleted: reported

Deleted: Our results are associated with relatively low uncertainties reaching a maximum of 4239% based on the used Gaussian inverse model and 101% based on prior emission ensemble; ...w

Deleted: w

Deleted: independent

Deleted: -based

Deleted: different

Deleted: the posterior emissions of ammonia calculated with

Deleted: and

Deleted: combined with our adapted inverse modelling framework...

Deleted: constitute

Deleted: basis for European NH₃

Deleted: show the *de facto*

Deleted: since 2013

1 Introduction

Ammonia (NH_3), the only alkaline gas in the atmosphere, constitutes one of the most reactive nitrogen species. It is produced from decomposition of urea, which is a rapid process when catalyzed by enzymes (Sigurdarson et al., 2018). The main sectors contributing to its production are livestock management and wild animals (Behera et al., 2013), biomass burning and domestic coal combustion (Fowler et al., 2004; Sutton et al., 2008), volcanic eruptions (Sutton et al., 2008), and agriculture (Erisman et al., 2007). Emissions from agricultural activity and livestock management represent over 80% of the total emissions (Crippa et al., 2020), while their regional contribution can reach 94% (Van Damme et al., 2018).

Once emitted, it is transported over short distances and deposited to water bodies, soil or vegetation with a typical atmospheric lifetime of a few hours (Evangelizou et al., 2021). It can then lead to eutrophication of water bodies (Stevens et al., 2010), modulate soil pH (Galloway et al., 2003) and «burn» vegetation by pulling water from the leaves (Krupa, 2003). It also reacts with the abundant atmospheric sulfuric and nitric acids (Malm, 2004) forming fine particulate matter ($\text{PM}_{2.5}$) (Tsimpidi et al., 2007). While ammonia has a short atmospheric lifetime, $\text{PM}_{2.5}$ resides significantly longer in the atmosphere, on the order of days to weeks (Seinfeld and Pandis, 2000), and hence is transported over longer distances. Accordingly, secondary $\text{PM}_{2.5}$ can affect the Earth's radiative balance, both directly by scattering incoming radiation (Henze et al., 2012) and indirectly as cloud condensation nuclei (Abbatt et al., 2006). Its environmental effects include visibility problems and contribution to haze formation. Finally, $\text{PM}_{2.5}$ affects human health, as it penetrates the human respiratory system and deposits in the lungs and alveolar regions (Pope and Dockery, 2006; Pope III et al., 2002) contributing to premature mortality (Lelieveld et al., 2015).

To combat secondary pollution, the European Union established a set of measures focusing on ammonia abatement, similar to the ones introduced by China (Giannakis et al., 2019). These measures aim at reducing ammonia emissions by 6% in 2020, relative to 2005. However, the lack of spatiotemporal measurements of ammonia over Europe makes any assessment of the efficiency of these measures difficult, as only bottom-up methods are used to calculate emission. These methods still show a slight increase ($0.6\% \text{ y}^{-1}$) up to 2018 mostly due to increasing agricultural activities (McDuffie et al., 2020). Such bottom-up approaches rely on uncertain land-use data and emission factors that are not always up to date, thus adding large errors to existing inventories.

113 During the last decade, satellite products have also become available to fill the gaps
114 created by spatially disconnected ground-based measurements. Data from satellite sounders
115 such as the Infrared Atmospheric Sounding Interferometer (IASI) (Van Damme et al., 2017),
116 the Atmospheric Infrared Sounder (AIRS) (Warner et al., 2017), the Cross-track Infrared
117 Sounder (CrIS) (Shephard and Cady-Pereira, 2015), the Tropospheric Emission Spectrometer
118 (TES) (Shephard et al., 2015), and Greenhouse Gases Observing Satellite (GOSAT) (Someya
119 et al., 2020) are publicly available. Most of them have been validated against ground-based
120 observations or complemented with other remote sensing products (Van Damme et al., 2015,
121 2018; Dammers et al., 2016, 2017, 2019; Kharol et al., 2018; Shephard et al., 2020; Whitburn
122 et al., 2016).

123 Accordingly, a few studies on ammonia emission calculations have been recently
124 published relying on 4D-Variational inversion schemes such as (Cao et al., 2022; Zhu et al.,
125 2013) or process based models (Beaudor et al., 2023; Vira et al., 2020). More recently, Sitwell
126 et al. (2022) proposed an inversion scheme for [comparison between model profiles and satellite](#)
127 [retrievals using hybrid logarithmic and linear observation operator that attempts to choose the](#)
128 [best method according to the particular situation](#). In the present study, we use direct
129 comparisons between the CrIS [ammonia retrievals](#) and model [profiles](#) using the Least Squares
130 with Adaptive Prior Covariance (LS-APC) algorithm (Tichý et al., 2016), which reduces the
131 number of tuning parameters in the method significantly using variational Bayesian
132 approximation technique. We constrain ammonia emissions over Europe over the 2013–2020
133 period and validate the results against ground-based observations from EMEP (European
134 Monitoring and Evaluation Programme, <https://emep.int/mscw/>) (Torseth et al., 2012).

135 2 Methods

136 2.1 CrIS observations

137 To constrain ammonia emissions with inverse modelling, satellite measurements were
138 adopted from the Cross-Track Infrared Sounder (CrIS) onboard the NASA Suomi National
139 Polar-orbiting Partnership (S-NPP) satellite, which provides atmospheric soundings with a
140 spectral resolution of 0.625 cm^{-1} (Shephard et al., 2015). CrIS presents improved vertical
141 sensitivity for ammonia closer to the surface due to the low spectral noise in the ammonia
142 spectral region (Zavalyov et al., 2013) and the early afternoon overpass that typically coincides
143 with high thermal contrast, which is optimal for thermal infrared sensitivity. The CrIS Fast
144 Physical Retrieval (CFPR) (Shephard and Cady-Pereira, 2015) retrieves ammonia profiles at

Formatted: Font: (Default) Times New Roman

Deleted: a non-linear CrIS observation model using
alternation between CrIS ammonia retrievals performed with
the logarithm of concentrations and linearized retrievals

Deleted:

Deleted: observations

Deleted: retrievals

Formatted: Font: (Default) Times New Roman

151 14 levels using a physics-based optimal estimation retrieval, which also provides the vertical
 152 sensitivity (averaging kernels) and an estimate of the retrieval errors (error covariance matrices)
 153 for each measurement. As peak sensitivity typically occurs in the boundary layer between 900
 154 and 700 hPa (~ 1 to 3 km) (Shephard et al., 2020) and the surface and total column
 155 concentrations are both highly correlated with these boundary layer retrieved levels. The total
 156 column random measurement error is estimated in the 10–15% range, with total errors to be
 157 ~30% (Shephard et al., 2020). The individual profile retrieval levels show an estimated random
 158 measurement error of 10–30 %, with total random errors estimates increasing to 60 to 100%
 159 due to the limited vertical resolution (1 degree of freedom of signal for CrIS ammonia). These
 160 vertical sensitivity and error output parameters are also useful for using CrIS observations in
 161 applications (e.g. data fusion, data assimilation; model-based emission inversions; (Cao et al.,
 162 2020; Li et al., 2019)), as a satellite observational operator can be generated in a robust manner.
 163 The detection limit of CrIS measurements has been calculated down to 0.3–0.5 ppbv (Shephard
 164 et al., 2020). CrIS ammonia has been evaluated against other observations over North America
 165 with the Ammonia Monitoring Network (AMoN) (Kharol et al., 2018) and against ground-
 166 based Fourier transform infrared (FTIR) spectroscopic observations (Dammers et al., 2017)
 167 showing small bias and high correlations.

168 Daily CrIS ammonia (version 1.6.3) was interpolated onto a 0.5°×0.5° grid covering all
 169 of Europe (10°W–50°E, 25°N–75°N) for the period 2013–2020. Interpolation was chosen due
 170 to the large number of observations (around 10,000 retrievals per day per vertical level), which
 171 made the calculation of source-receptor matrices (SRMs) computationally inefficient. Through
 172 interpolation we limited the number of observation (and thus the number of SRMs to be
 173 calculated) to 2000 per day per vertical level. Sitwell et al. (2022) showed that the averaging
 174 kernels of CrIS ammonia are significant only for the lowest six levels (the upper eight have no
 175 influence onto the satellite observations) and therefore we considered only these six vertical
 176 levels (~1018–619 hPa).

177 2.2 A priori emissions of ammonia

178 We used as a priori emissions for ammonia in the inversion algorithm the ones calculated
 179 (i) from the most recent version of ECLIPSEv6 (Evaluating the CLimate and Air Quality
 180 ImPacts of Short-livEd Pollutants) (Klimont, 2022; Klimont et al., 2017) combined with
 181 biomass burning emissions from GFEDv4 (Global Fire Emission Dataset) (Giglio et al., 2013)
 182 hereafter “EC6G4”, (ii) a more traditional dataset from ECLIPSEv5, GFEDv4 and GEIA
 183 (Global Emissions InitiAtive), hereafter “EGG” (Bouwman et al., 1997; Giglio et al., 2013;

Deleted:

Deleted: random

Deleted: estimates

Deleted: of

Deleted: consisting of 2920 retrievals

Deleted: 1

Deleted: for 6

Deleted: s

192 Klimont et al., 2017), (iii) emissions calculated from IASI (Infrared Atmospheric Sounding
193 Interferometer) and a 1-dimensional box-model and a modelled lifetime (Evangelou et al.,
194 2021), denoted as “NE” and (iv) from the high resolution dataset of Van Damme et al. (2018)
195 after applying a simple 1-dimensional box-model (Evangelou et al., 2021), hereafter denoted
196 as “VD”. Given the large uncertainty in ammonia emissions illustrated in [Figure 1](#), we
197 calculated the average of these four priors (hereafter “avgEENV”) to establish the a priori
198 emissions used in this study.

Deleted: Figure 1

199 2.3 Lagrangian particle dispersion model for the calculation of source-receptor 200 matrices (SRMs) of ammonia

201 SRMs were calculated for each $0.5^\circ \times 0.5^\circ$ grid-cell over Europe (10°W – 50°E , 25°N –
202 75°N) using the Lagrangian particle dispersion model FLEXPART version 10.4 (Pisso et al.,
203 2019) adapted to simulate ammonia. The adaptation of the code includes treatment for the loss
204 processes of ammonia adopted from the Eulerian model LMDZ-OR-INCA (horizontal
205 resolution of $2.5^\circ \times 1.3^\circ$ and 39 hybrid vertical levels) that includes all atmospheric processes
206 and a state-of-the-art chemical scheme (Hauglustaine et al., 2004). The model accounts for
207 large-scale advection of tracers (Hourdin and Armengaud, 1999), deep convection (Emanuel,
208 1991), while turbulent mixing in the planetary boundary layer (PBL) is based on a local second-
209 order closure formalism. The model simulates atmospheric transport of natural and
210 anthropogenic aerosols and accounts for emissions, transport (resolved and sub-grid scale), and
211 dry and wet deposition. LMDZ-OR-INCA includes a simple chemical scheme for the ammonia
212 cycle and nitrate particle formation, as well as a state-of-the-art $\text{CH}_4/\text{NO}_x/\text{CO}/\text{NMHC}/\text{O}_3$
213 tropospheric photochemistry (Hauglustaine et al., 2014). To calculate chemical loss of
214 ammonia to $\text{PM}_{2.5}$, after a month of spin-up, global atmospheric transport of ammonia was
215 simulated for 2013–2020 by nudging the winds of the 6-hourly ERA Interim Reanalysis data
216 (Dee et al., 2011) with a relaxation time of 10 days (Hourdin et al., 2006). Using the EGG
217 inventory, we calculated the e-folding lifetime of ammonia in the model, which was adopted in
218 FLEXPART. We refer the reader to (Tichý et al., 2022) for a detailed description of the
219 formalism. Atmospheric linearities of the system and a full validation against ground-based
220 observation are also presented in the same paper.

221 FLEXPART releases computational particles that are tracked backward in time using
222 ERA5 (Hersbach et al., 2020) assimilated meteorological analyses from the European Centre
223 for Medium-Range Weather Forecasts (ECMWF) with 137 vertical layers, a horizontal
224 resolution of $0.5^\circ \times 0.5^\circ$ and [one hour temporal resolution](#). FLEXPART simulates turbulence

Deleted: a temporal hourly one

(Cassiani et al., 2014), unresolved mesoscale motions (Stohl et al., 2005) and includes a deep convection scheme (Forster et al., 2007). SRMs were calculated for 7 days backward in time, at temporal intervals that matched satellite measurements and at spatial resolution of $0.25^\circ \times 0.25^\circ$. This 7-day backward tracking is sufficiently long to include almost all ammonia sources that contribute to surface concentrations at the receptors given a typical atmospheric lifetime of about half a day (Van Damme et al., 2018; Evangeliou et al., 2021).

2.4 Inverse modeling algorithm

The inversion method used in the present study relies on optimization of the difference between the CrIS satellite vertical profile observations, denoted as v^{sat} , and retrieved vertical profile, v^{ret} . The latter are obtained by applying an instrument operator applied in logarithm space (Rodgers, 2000) as follows:

$$\ln(v^{ret}) = \ln(v^a) + A(\ln(v^{true}) - \ln(v^a)) \quad (1)$$

where v^{ret} is the retrieved profile concentration vector, v^a is a priori profile concentration vector used in the satellite retrievals, v^{true} is the hypothetical true profile concentration vector supplied by the model ($v^{true} = v^{mod}$), and A is the averaging kernel matrix (for each $0.5^\circ \times 0.5^\circ$ resolution grid-cell). Eq. (1) provides a useful basis for the calculation of the CrIS retrievals if the retrieval algorithm is performing as designed, i.e., it is unbiased and the root mean square error (RMSE) is within the expected variability. The v^{mod} term can be written as:

$$v^{mod} = Mx \quad (2)$$

for each grid-cell of the spatial domain, where M is the grid-cell specific SRM calculated with FLEXPART and x is the unknown grid-cell specific emission vector. The SRM matrix M is calculated on circular surroundings around each grid-cell for computational efficiency. We chose circles with a radius of approximately 445 km, equal to 4 degrees, which is shown to be sufficient for reliable emission estimation and low sensitivity has been observed with this choice. Since the vector x is unknown, we replace it by a prior emission x^a (see section 2.2) in the initial step that is gradually refined iteratively based on the satellite observations.

The used inversion setup is based on iterative minimization of mismatch between v^{sat} and v^{ret} updating (iteratively) the emission x such as below:

$$\arg \min_{x^a \rightarrow x} \|v^{sat} - v^{ret}\|_2^2 \quad (3)$$

for each grid-cell of computational domain. The minimization problem is solved in two steps.

First, we construct the linear inverse problem for each year where v^{ret} from the given surroundings, denoted here as S , forms the block-diagonal matrix v_s^{ret} while v^{sat} from the

Deleted: distance

Deleted: The CrIS satellite retrieved observations are in situ profiles with...

Deleted: a

Deleted: This is a useful technique

Deleted: evaluating

Deleted: due to

Deleted: effectiveness

Deleted: We select 4 degrees radius surroundings (approx. 445 kilometers)...

Formatted: Font: (Default) Times New Roman

Formatted: Font: (Default) Times New Roman

Deleted: distance

Deleted: mismatch

given surroundings form an associated observation vector v_S^{sat} . This forms the linear inverse problem:

$$v^{sat} = v_S^{ret} q_S \quad (4)$$

where the vector q_S is a vector with coefficients denoting how x^a needs to be refined to obtain emission estimate vector x . For one year, 6 vertical profiles, and 4 degrees radius, the size of the the block-diagonal matrix v_S^{ret} is 13896 times 12, hence, the correction coefficient vector q_S contain 12 values corresponding to each month. We solve Eq. 4 using the least squares with adaptive prior covariance (LS-APC) algorithm (Tichý et al., 2016). The algorithm is based on variational Bayesian methodology assuming non-negative solution and favoring solution without abrupt changes and it minimizes the use of manual tuning (Tichý et al., 2020). The method assumes the data model in the form of:

$$p(v^{sat}) = N(v_S^{ret} q_S, R) \quad (5)$$

where N denotes the multivariate normal distribution and R the covariance matrix assumed in the form $R = \omega^{-1} I_p$ with unknown precision parameter ω on its diagonal. Following Bayesian methodology, we assign prior model to all unknown parameters, i.e. ω and q_S . Their prior models are selected as:

$$p(\omega) = G(\vartheta_0, \rho_0) \quad (6)$$

$$p(q_S) = tN(0, (LV L)^{-1}, [0, +\infty]) \quad (7)$$

where $G(\vartheta_0, \rho_0)$ is the Gamma distribution (conjugate to the normal distribution) with prior parameters ϑ_0, ρ_0 selected to 10^{-10} achieve non-informative prior. The second term follows truncated normal distribution with positive support and with specific form of a precision matrix. We assume the precision matrix in the form of modified Cholesky decomposition which allows for tractability of estimation of its parameters, matrices V and L . The matrix V is diagonal with unknown diagonal parameters and the matrix L is lower bidiagonal with ones on the diagonal and unknown parameters on its sub-diagonal, formalized as vectors v and l , respectively. These parameters are estimated within the method, while purpose of vector v is to allow for abrupt changes in q_S , and vector l to favor smooth estimates (see details in Tichý et al., (2016)). All model parameters (ω, q_S, v, l) are estimated using the variational Bayes procedure where we obtain not only point-estimates, but their full posterior distributions.

Second, the grid-cell specific coefficient vector q_S is propagated through Eq. 2 into Eq. 1 to refine a prior emission x^a and obtain estimated unknown emissions x . To maintain stability of the method, we bound the ratio between prior and posterior emission elements to 0.01 and 100, respectively. This choice, motivated by Cao et al. (2020), omits unrealistically small or

Formatted: Font: (Default) Times New Roman

Deleted: ¶¶¶

Deleted: ¶¶

Formatted: Font: (Default) Cambria,

Deleted: 4

Deleted: ,

Deleted: (¶¶)

Deleted: is

Deleted: 4

Deleted: 4

Deleted: The second term follows truncated normal distribution with positive support and with specific form of precision matrix as the modified Cholesky decomposition with diagonal matrix V with unknown parameters on its diagonal and lower bidiagonal matrix L with ones on the diagonal and unknown parameters on its sub-diagonal, formalized as vectors v and l respectively.

Deleted: while

Deleted: , see

Deleted: discussion

Deleted: (

Deleted: ,

Deleted: (Tichý et al., 2016

325 high emissions, however, the bounds are large enough to allow for new sources, as well as for
326 attenuation of old sources. To introduce these boundaries is necessary since the problem in Eq.
327 1 is ill-conditioned and the propagation through the equation may lead to unrealistic values due
328 to numerical instability. For this reason, these boundaries are needed and the sensitivity to the
329 choice of the prior emission are studied in Section 3.3.

Deleted: the choice of prior emission is of great importance in the method...

Deleted: will be

330 Note that CrIS data for some spatiotemporal elements are missing in the dataset. In these
331 cases, we interpolated the missing data following the method proposed by D’Errico (2023),
332 which solves a direct linear system of equations for missing elements, while the extrapolation
333 behavior of the method is linear. Another strategy recently adopted in the literature has been to
334 tackle the missing data using total variation methodology (see details in Fang et al., 2023);
335 however, the method has been limited so far to its use on point-source release, hence we did
336 not use it in this work.

Deleted: NaN

337 3 Results

338 3.1 Emissions of ammonia in Europe (2013–2020)

339 We analyze the CrIS ammonia satellite observations for Europe (10°W–50°E, 25°N–
340 75°N) over the 2013-2020 period on monthly basis to derive ammonia emissions using the
341 inverse modelling methodology described in Section 2.4. The inversion algorithm is applied to
342 each year of CrIS observations separately with the use of the avgEENV prior emission.

343 The overall resulting spatial distribution of the posterior emissions of ammonia (denoted
344 as `posterior_avgEENV`) averaged for the whole period are displayed in Figure 2 (top-left). The
345 highest emissions occur in Northwestern Europe (including Northern Belgium, the Netherlands
346 and northwestern Germany) and to a smaller extent in the Po Valley (Italy), and the Ebro Valley
347 (Spain). Local maxima are also seen over Pulawy (Poland), South Romania and Kutina
348 (Croatia) due to industrial applications (Clarisse et al., 2019; Van Damme et al., 2018). While
349 ammonia emissions were not calculated high in the Po Valley (8 year average), it has been
350 reported that in Lombardy, about 90% of the ammonia emissions there have been reported to
351 originate from manure management (Lonati and Cernuschi, 2020). The Ebro Valley is
352 characterized by intensive agricultural activities (Lassaletta et al., 2012; Lecina et al., 2010)
353 and the Aragon and Catalonia regions by large pig farms (Van Damme et al., 2022). Finally,
354 both Belgium and The Netherlands are countries in which intensive livestock activity is
355 documented. It consists mostly of dairy cow, beef cattle, pig and chicken farming (Gilbert et
356 al., 2018; Lesschen et al., 2011; Velthof et al., 2012).

Formatted: Body, Justified, Indent: First line: 1 cm, Line spacing: 1.5 lines

Deleted: Figure 2

362 [Figure 2](#) (top-right) shows the annual posterior emissions discretized monthly for the
 363 whole period (solid line) compared to prior ammonia emissions (dashed line), [averaged for the](#)
 364 [domain](#). Higher emissions [than](#) the prior ones were calculated, which is not necessarily
 365 attributed to emission increases over Europe, but rather to miscalculation of emissions in the
 366 prior bottom-up inventories that were used. A strong seasonal cycle is also observed peaking
 367 in the middle of each year (summer) of the study period, but for several of these years, the
 368 characteristic bimodal cycle also appears with another peak in spring (Beaudor et al., 2023).

369 To examine more closely the seasonal variability of ammonia emissions in Europe, we
 370 present the monthly posterior emissions of ammonia averaged for the whole study period
 371 (2013–2020) at the bottom-left panel of [Figure 2](#), together with the prior ones. [The total](#)
 372 [emissions for each month based on the map element size and length of the respective month](#)
 373 [were averaged for the whole study period. The same was done for each year in the bottom-right](#)
 374 [panel](#). The interannual variability over the period between 2013 and 2020, is also apparent in
 375 the monthly box and whisker plots of the posterior emissions. In addition, the spatial
 376 distribution of monthly ammonia emissions averaged for the eight-year period is given in
 377 [Supplementary Figure S 1](#). It appears that ammonia emissions are very low in wintertime (DJF
 378 average: 286 Gg) over Europe and increase towards summer (JJA average: 563 Gg), due to
 379 temperature dependent volatilization of ammonia (Sutton et al., 2013), with the largest
 380 emissions occurring in August (601 Gg). Although a clear peak of fertilization in early spring
 381 is missing from the plot, emissions start to increase in early spring to peak in late-summer (Van
 382 Damme et al., 2022) corresponding to the start and end of the fertilization periods in Europe
 383 (Paulot et al., 2014). Fertilization is tightly regulated in Europe (Ge et al., 2020). It is only
 384 allowed from February to mid-September in The Netherlands, while manure application is also
 385 only allowed during the same period depending on the type of manure and the type of land (Van
 386 Damme et al., 2022). In Belgium, nitrogen fertilizers are only allowed from mid-February to
 387 the end of August (Van Damme et al., 2022), so as in Germany (restricted in winter months)
 388 (Kuhn, 2017).

389 Finally, [Figure 2](#) (bottom-right) shows the annual posterior emissions for the whole
 390 period with the annual total emissions for each year. We observe a significant decrease in
 391 ammonia posterior emissions over Europe during the 2013–2020 period. Emissions were
 392 estimated as 5431 Gg for 2013 decreasing to 4890 Gg in 2014. A minor increase can be seen
 393 in 2015 (5104 Gg), after which a significant decrease of 534 Gg (more than 10%) was estimated,
 394 followed by the nearly constant plateau at the levels between 4383 Gg in 2017, 4323 Gg in
 395 2019 and finally to 3994 Gg in 2020. The gradual decrease in ammonia emissions over Europe

Deleted: Figure 2

Deleted: Figure 2

Deleted: For t

Deleted: his averaging, we calculate t

Deleted: is

Deleted: Supplementary Figure S 1

Deleted: Figure 2

since 2013 is also plotted spatially in [Supplementary Figure S 2](#). It is evident that the restrictions and measures adopted by the European Union to reduce secondary PM formation were successful, as emissions in the hot-spot regions of Belgium, The Netherlands, Germany and Poland declined drastically over time. However, an increase of +4.4% was observed in 2015. It has been reported that ammonia emissions increased in 2015 and several European Union Member States, as well as the EU as a whole, exceeded their respective ammonia emission ceilings (EEA, 2017). The increase was reported to be +1.8% and was mainly caused by increased emissions in Germany, Spain, France, and the United Kingdom. This was caused by extensive use of inorganic nitrogen fertilizers (including urea application) in Germany, while increased emissions in Spain were driven by an increase in the consumption of synthetic nitrogen fertilizers and in the number of cattle and pigs (EEA, 2017). It should be mentioned that a [false decrease of ammonia in 2020 due to the COVID-19 pandemic is calculated by the current methodology](#), mainly due to bias created by the decrease of NO_x and SO₂ that are precursor species of the atmospheric acids, with which ammonia reacts (see Tichý et al., 2022).

Deleted: Supplementary Figure S 2

Deleted: partial

Deleted: might be

3.2 Country by country ammonia emissions

Posterior annual emissions of ammonia for 2013–2020 are plotted for four European regions (Western, Central and Eastern, Northern and Southern Europe), [accompanied by relative trends calculated as difference between year 2013 and 2020 divided by the average for the whole period](#), in the left panel of [Figure 3](#), while the estimated seasonal variation of each region is shown on the right panels averaged over the whole eight-year period. Western Europe includes Ireland, Austria, France, Germany, Belgium, Andorra, Luxembourg, The Netherlands, Switzerland, and United Kingdom; Central and Eastern Europe include Albania, Bosnia and Herzegovina, Bulgaria, Czechia, Croatia, Hungary, Belarus, Slovakia, North Macedonia, Montenegro, Poland, Romania, Moldova, Slovenia, Ukraine, and Serbia; Northern Europe is defined by Denmark, Estonia, Finland, Latvia, Lithuania, Faroe Islands, Norway, and Sweden; finally, Southern Europe includes Cyprus, Greece, Italy, Portugal, Spain.

Deleted: Figure 3

The most significant decreases in ammonia emissions were estimated to be -38% in Central and Eastern Europe and -37% in Western Europe, respectively. Quantitatively, Central and Eastern Europe emissions were estimated to gradually drop from 2190 Gg in 2013 and to 1495 Gg in 2020 with a small increase in 2015 (2171 Gg) mainly because Germany, France and the United Kingdom missed their emission targets (EEA, 2017). Western European emissions of ammonia also declined constantly over time from 2041 Gg in 2013 to 1421 Gg in 2020. Smaller, yet significant, decreases were calculated over Northern Europe from 398 Gg in

2013 to 333 Gg in 2020 (-17%). Finally, Southern Europe exhibited a minor drop between years 2013 and 2014 (from 803 Gg in 2013 to 729 Gg in 2014) followed by a small increase until 2019 (from 729 to 803 Gg), and then decreased again in 2020 to 743 Gg. Overall, Southern European emissions decreased by -7.62%.

The seasonal cycle of ammonia was again characterized by the restrictions applied to the agricultural-related activities by the European Union member states (Figure 3, right panels). As such, emissions in Western, Central and Eastern and Southern Europe were very low in winter and started increasing when fertilization was allowed in early spring, whereas the increasing temperature towards summer increased volatilization and, thus, emissions of ammonia (Van Damme et al., 2022; Ge et al., 2020). Although much less marked than in other European regions due to lower prevailing temperatures and weaker agricultural applications, emissions in Northern Europe show the spring-summer temperature dependence. However, emissions were estimated to be double in winter rather following the cycle of SO₂ (Tang et al., 2020). Emission may increase in Northern Europe in winter because OH and O₃ concentrations are much lower, and the rate of converting SO₂ to sulfate much slower. This means that less sulfate is produced and thus more NH₃ stays in the gas form. Supplementary Figure S 3 shows prior emissions in Western, Central and Eastern, Northern and Southern Europe for EC6G4 and NE emission inventories. Both show the aforementioned increase in emissions during winter in Northeastern Europe. Specifically, the NE emissions that dominate the a priori emissions (avgEENV), as the highest inventory, show an extreme winter peak in the north (emissions decline from 105 to 13 Gg). Therefore, there is a very strong dependence of the posterior seasonality of ammonia in Northern Europe, which may be also influenced by the used prior emissions, see uncertainty analysis in Section 3.3.

Country specific emissions of posterior ammonia on a monthly basis (eight-year average emissions) are shown for 20 countries in Supplementary Figure S 4. For countries such as Portugal, Spain, Italy, United Kingdom, The Netherlands, Belgium, Poland, Hungary, Denmark, Belarus and Romania two peaks can be clearly seen in late spring and end of summer. As discussed before, these peaks coincide with the two main fertilization periods in Europe (Paulot et al., 2014). However, it is expected that ammonia abundance is high throughout the entire spring–summer period (e.g., Greece, France, Germany, Czechia, Ukraine and Bulgaria) due to agricultural activity and temperature dependent volatilization (Sutton et al., 2013). Ammonia emissions in Finland, Sweden and Norway are smaller than in the rest of Europe and show a reverse seasonality.

Formatted: Body

Deleted: Figure 3

Deleted: Despite measurements have shown that ammonia might increase in winter at high latitudes (Aas et al., 2020), we conclude that the model likely underperforms here. ...

Deleted: Supplementary Figure S 3

Deleted: Especially

Deleted: that were used here

Deleted: ,

Deleted: because they are

Deleted: , whereas the

Deleted: is extreme

Deleted: 35

Deleted: 12

Deleted: due to the strong prior that we use there

Deleted: Supplementary Figure S 4

3.3 Uncertainties in ammonia's posterior emissions

For the calculation of uncertainty of the estimated posterior emissions two different approaches were used. The first approach is based on uncertainty arising as a result of the inversion methodology. The standard deviation is calculated from posterior estimate which is in the form of Gaussian distribution such as

$$p_{\text{posterior}}(x_i) = N(\mu_i, \sigma_i^2) \quad (8)$$

where N denotes normal (Gaussian) distribution and posterior parameters μ_i and σ_i are results of inversion for each element of the spatiotemporal domain. The uncertainty associated with any given spatial element is then a property of Gaussian distribution define with the square root of summed squared standard deviations:

$$\Sigma_{\text{location}} = \sqrt{\sum_t \sigma_{\text{location},t}^2} \quad (9)$$

Here, we consider uncertainty calculated as 2σ standard deviations, i.e. 95% of the values lay inside the interval with the center in the reported emissions surrounded by the reported uncertainty.

The second approach is based on ensemble of the used prior emissions as an input for the inversion. The different ensemble members are built from five prior emissions (see Figure 1) while the uncertainty is calculated as the standard deviation of five resulting posterior emissions.

The calculated posterior uncertainty for our spatial domain and studied period (2013–2020) is shown in Figure 4 (right). The uncertainty associated with Gaussian posterior for each year of the study period are depicted in Supplementary Figure S 5. The absolute uncertainty of Gaussian posterior ammonia emissions reaches a maximum of 23.3 ng m⁻² s⁻¹ or about 39% (relative value, calculated based on related maximum of posterior emissions). The uncertainty based on prior ensemble reaches a maximum of 60.2 ng m⁻² s⁻¹ which is equal to about 101% based on related maximum of posterior emissions. In general, the pattern of both posterior uncertainties, Gaussian posterior and prior ensemble respectively, are in agreement in their patterns and follow the one of the posterior emissions, with the highest values over (i) Belgium, the Netherlands, and Germany due to livestock, farming, and agricultural activity; (ii) Poland, South Romania and Croatia due to industrial applications; (iii) Catalonia due to pig farming; (iv) West France due to manure application. Nevertheless, the obtained posterior uncertainty remains low, and this depicts the robustness of the methodology used and the calculated posterior emissions of ammonia.

Deleted: We use two different ways f

Deleted: 7

Formatted: Indent: First line: 0 cm

Deleted: our

Deleted: al-

Deleted: given using

Deleted: as a

Deleted: .

Deleted: 7

Deleted: ,

Deleted: Fig. 1

Deleted: ,

Deleted: For the calculation of uncertainty of posterior emissions of ammonia, we benefit from the form of posterior, which arises as a Gaussian distribution with calculated mean and standard deviation for each element of our spatiotemporal domain. In accordance with the posterior emissions defined in Section

Deleted: 2.4

Deleted: , we propagate the standard deviation through Eq. 1 to obtain the uncertainty of each spatiotemporal element, here denoted as . If two variables follow a Gaussian distribution with means and and standard deviations and , the sum of these variables has the mean and standard deviation . Therefore, the total uncertainty for each spatial element over the temporal axis is then a square root of summed uncertainties over the selected time steps : (

Deleted: 5

Deleted:)

Deleted: Figure 5 for Gaussian posterior (left) and for ensemble of prior emissions...

Deleted: Here, we display uncertainty calculated as 2 standard deviations (2), i.e. 95% of the values lay inside the interval with the center in the reported emission surrounded by the reported uncertainty.

Deleted:

Deleted: same results

Deleted: Supplementary Figure S 4

Deleted: 25

Deleted: 42

Deleted: uncertainty

Deleted: s

3.4 Validation of posterior emissions

As shown in Eq. 3 (Section 2.4), the inversion algorithm minimizes the distance between the satellite observations (v^{sat}) and the retrieved ammonia concentrations (v^{ret}). The latter is a function of different satellite parameters (e.g., averaging kernel sensitivities) and modelled ammonia concentrations using a prior dataset (v^{mod} or v^{true}) as seen in Eq. 1. The overall result is always propagated to v^{mod} iteratively, each time updating the prior emissions to obtain posterior ammonia. As specified in CrIS guidelines, modelled concentrations (v^{mod}) cannot be directly compared with satellite data (v^{sat}), while comparing v^{sat} with v^{ret} is not a proper validation method, because the comparison is performed for satellite observations that were included in the inversion (dependent observations), and the inversion algorithm has been designed to reduce the v^{sat} - v^{ret} mismatches. This means that the reduction of the posterior retrieved concentration (v^{ret}) mismatches to the observations (v^{sat}) is determined by the weighting that is given to the observations with respect to v^{ret} . A proper validation of the posterior emissions is performed against observations that were not included in the inversion (independent observations).

For these reasons, we compare modelled posterior concentrations of ammonia (v^{mod}) at the surface with ground-based observations over Europe from the EMEP (European Monitoring and Evaluation Programme, <https://emep.int/mscw/>) network (Torseth et al., 2012). The measurements are open in public and can be retrieved from <https://ebas.nilu.no>. We used measurements for all years between 2013 and 2020 from an average of 53 stations with 2928 observations for each station covering all Europe (Supplementary Figure S 6). The comparison is plotted for each of the 53 stations separately on a Taylor diagram in Figure 5. For all stations, the Pearson's correlation coefficient increased for the posterior ammonia (coloured circles) increased as compared to the prior one (coloured squares) reaching above 0.6 at several stations, while the normalized root mean square error (nRMSE) and standard deviation were kept below 2 (unitless) and 2 $\mu\text{g m}^{-3}$, respectively, in almost all stations (except SI0008 in Slovenia).

To further show how posterior emissions of ammonia affect modelled concentrations, we chose six stations (DE0002 in Germany, NO0056 in South Norway, ES0009 in Spain, NL0091 in the Netherlands, HU0002 in Hungary and PL0005 in Poland) from the EMEP network (highlighted in red in Supplementary Figure S 6), and we plot prior and posterior concentrations against ground-based ammonia over time for the whole study period (2013–2020) in Supplementary Figure S 7. Given the long period of plotting, we average observations every week and modelled concentrations every month for a more visible representation of the

Deleted: ¶

Deleted: Supplementary Figure S 6

Deleted: Figure 6

Deleted: Supplementary Figure S 6

Deleted: Supplementary Figure S 7

600 comparison. To evaluate the comparison, we calculate a number of statistic measures, namely
 601 nRMSE, the normalized mean absolute error (nMAE) and the root mean squared logarithmic
 602 error (RMSLE) as defined below:

$$603 \quad nRMSE = \sqrt{\frac{\sum_{i=1}^n \frac{1}{n} (m_i - o_i)^2}{\frac{1}{n} \sum_{i=1}^n o_i}} \quad nMAE = \frac{\sum_{i=1}^n |m_i - o_i|}{\sum_{i=1}^n o_i}$$

$$604 \quad RMSLE = \sqrt{\frac{1}{n} \sum_{i=1}^n (\log m_i - \log o_i)^2} \quad (11)$$

605 where n is sample size, m and o the individual sample points for model concentrations and
 606 observations of ammonia indexed with i . As one can see in [Supplementary Figure S 7](#), all
 607 statistics were improved in all six stations and posterior concentrations were closer to the
 608 observations. However, individual peaks were in many cases misrepresented in the model.
 609 Whether this is a result of the measurement technique or the fact that local sources cannot be
 610 [resolved at the](#) spatiotemporal resolution [of](#) CTM and FLEXPART (given the short lifetime of
 611 atmospheric ammonia) needs further research. The best results were obtained at station ES0009
 612 (Spain), where model captures the seasonal variation of the observations during the whole study
 613 period (2013–2020). In all other stations, the seasonality is maintained albeit steep peaks in the
 614 observations are lost.

615 4 Discussion

616 4.1 Comparison with emissions inferred from satellite observations

617 We compared our posterior estimates with two recently published studies on ammonia
 618 emission in Europe (Cao et al., 2022; Luo et al., 2022). Luo et al. (2022) used IASI observations
 619 for the period 2008 to 2018 to estimate ammonia emissions in a global domain. Their method
 620 was based on updating prior emissions with correction term computed using differences
 621 between observed and simulated ammonia columns combined with calculated ammonia
 622 lifetimes. The key indicators calculated for the European domain in Luo et al. (2022) are a
 623 linear trend for the 2008–2018 period, average annual emissions, and relative trends. Note that
 624 we compare our eight-year period with a decade in Luo et al. (2022). The comparison is
 625 depicted in [Figure 6](#). Our estimates ([Figure 6](#), left panel) are in good agreement with those
 626 calculated by Luo et al. (2022). The linear trend was estimated as -1.27 Tg for the period by
 627 Luo et al. (2022), while our estimate is -1.44 Tg. The spatial distribution of the trend is also
 628 given in [Figure 6](#), (left panel). The key decrease is observed mainly in France, Germany, and
 629 middle Europe, while the increasing trend is observed mostly in Spain, parts of Italy, and

Deleted: 6

Deleted: Supplementary Figure S 7

Deleted: considered for such high

Deleted: as those in the

Formatted: Default Paragraph Font, Font: (Default) Calibri, 13 pt, Underline colour: Custom Colour (RGB(79,129,189)), Font colour: Text 1, Text Outline

Formatted: Heading 2, Left, Indent: First line: 0 cm

Deleted: Figure 4

Deleted: Figure 4

Deleted: Figure 4

637 Greece. The average annual ammonia emission for the European domain in Luo et al. (2022)
638 was estimated to be 5.05 Tg while our estimate is 4.63 Tg. Our lower estimate (by
639 approximately 8%) may be attributed to use of more recent period considered in our study, but
640 both methods agree that the trend in Europe is negative. The relative decrease estimated by Luo
641 et al. (2022) is -25.1%, while we calculate -31.02%, which is again in very good agreement.

642 Cao et al. (2022) used CrIS observations for the year 2016 in order to estimate ammonia
643 emissions for 25 European Union members (EU25), namely Austria, Belgium, Bulgaria,
644 Croatia, Republic of Cyprus, Czech Republic, Denmark, Estonia, France, Germany, Greece,
645 Hungary, Ireland, Italy, Latvia, Lithuania, Luxembourg, Malta, Netherlands, Poland, Portugal,
646 Romania, Slovakia, Slovenia, and Spain. The method was tested with uni-directional and bi-
647 directional flux schemes. The uni-directional dry deposition scheme assumes only air to surface
648 exchange of ammonia ignoring changes in environmental conditions, while the bi-directional
649 scheme captures dynamics in measured ammonia fluxes. Total estimated ammonia emissions
650 for the EU25 region by the uni-directional scheme (posterior_uni) and the bi-directional scheme
651 (posterior_bi) were reported as 3534 Gg N y⁻¹ and 2850 Gg N y⁻¹, respectively. The
652 posterior_bi estimate is very close to our estimate for EU25 for the year 2016, which is 2712
653 Gg N y⁻¹, while the posterior_uni is approximately 30% higher. A uni-directional dry
654 deposition scheme ignores the impacts of changes in environmental conditions (e.g., soil
655 temperature, soil wetness, soil pH, fertilized condition, and vegetation type) on ammonia
656 emissions from fertilized soil and crops (volatilization), which likely lead to high biases in top-
657 down estimates. Ammonia in LMDz-OR-INCA model, that was used to capture ammonia's
658 losses, resembles a partially bi-directional treatment, where emissions and deposition are both
659 possible at the same time without any use of a compensation point; this may explain the 30%
660 difference.

661 The detailed EU25 emissions for the year 2016 are displayed in Figure 6, (right panel) for
662 posterior_uni (red), posterior_bi (yellow), our post_avgEENV (blue), and priors used by Cao
663 et al. (2022) and in our study (dashed red and blue, respectively). As seen from Figure 6, our
664 posterior estimates (post_avgEENV) have more similar characteristics with posterior_bi, with
665 monthly difference to be less than factor of 2 positive or negative from Cao et al. (2022). Note
666 that the posterior_uni estimates are always a factor of 3 higher than our posterior estimates for
667 ammonia emissions. The main differences can be observed during February-March and
668 October-November periods where our estimates are generally lower than those from Cao et al.
669 (2022).

Deleted: treats surface exchange of ammonia between the atmosphere and biosphere in a one-way manner (from air to surface) and ...

Deleted: Figure 4

Deleted: Figure 4

4.2 Assessment of ammonia's atmospheric linearities

Ammonia is a particularly interesting substance due to its affinity to react with atmospheric acids producing secondary aerosols. In most cases, it is depleted by sulfuric and nitric acids. In acidic atmospheres where total ammonia (TA=gas, aqueous and solid) is less than twice the total sulfate ($[TA] < 2[TS]$), all the available ammonia is taken up by the aerosol phase. In ammonia-rich environments ($[TA] > 2[TS]$), the excess ammonia reacts with nitric acid forming ammonium nitrate. If RH is too high, ammonium nitrate is aqueous (Seinfeld and Pandis, 2000). As ammonia reacts with sulfate, it neutralizes sulfuric acid decreasing its concentration. Part of the sulfate may be replaced by nitric acid increasing ammonium nitrate content in the aerosol. If RH is high and particles are aqueous, the sulfate that reacts with ammonia and decreases, increases the equilibrium vapor pressure of ammonia with nitric acid shifting the reaction towards production of free ammonia (Seinfeld and Pandis, 2000). However, production of ammonia is a rare event and lots of prerequisites must be fulfilled in order to take place.

The latter is illustrated in Supplementary Figure S 8a that shows the frequency distribution of gain (negative numbers) or loss (positive numbers) due to all chemical processes affecting ammonia into the inversion domain (10°W – 50°E , 25°N – 75°N), for the study period (2013 – 2020) and the lowest sigma-p vertical levels (~ 1018 – 619 hPa) that were significant in satellite observations (see averaging kernels in section 2.1) (Sitwell and Shephard, 2021). The figure shows mostly positive numbers indicating that atmospheric ammonia reacts towards secondary aerosol formation. The spatial distribution of gain/loss of ammonia is shown in Supplementary Figure S 8b. The pixels indicating production of gaseous ammonia are located in marine regions, where we chose to not perform inversions, as they are an order of magnitude lower (Bouwman et al., 1997), thus less significant. No continental pixels showing gain of ammonia were detected, which would cause simulated backwards in time to fail with our Lagrangian model (see next paragraph). Our approximation, although simplistic, provides computational efficiency when simulating SRMs in backward mode using FLEXPART (Pisso et al., 2019).

Seibert and Frank (2004) reported that standard Lagrangian particle dispersion models cannot simulate non-linear chemical reactions. However, all the other processes occurring during the atmospheric transport of trace substances are linear, i.e., advection, diffusion, convective mixing, dry and wet deposition, and radioactive decay. First-order chemical reactions, where the reaction rates can be prescribed, are also linear. Non-linear chemistry cannot be calculated because neither the background chemistry is modeled nor is the coupling

Formatted: Default Paragraph Font, Font: Calibri, Font colour: Text 1

Formatted: Default Paragraph Font, Font: Calibri, Font colour: Text 1

Formatted: Heading 2, Left, Indent: First line: 0 cm

Formatted: None, Font: Times New Roman

Formatted: None, Font: Times New Roman

Formatted: None, Font: Times New Roman

Formatted: None, Font: Times New Roman

Formatted: Font: (Default) Times New Roman, Font colour: Auto

Formatted: None, Font: Times New Roman

Formatted: None, Font: Times New Roman

Formatted: None, Font: Times New Roman

Formatted: None, Font: Times New Roman

Formatted: Font: (Default) Times New Roman, Font colour: Auto

Formatted: None, Font: Times New Roman

Formatted: None, Font: Times New Roman

Formatted: None, Font: Times New Roman

Formatted: None, Font: Times New Roman

Formatted: None, Font: Times New Roman

Formatted: None, Font: Times New Roman

Formatted: None, Font: Times New Roman

Formatted: None, Font: Times New Roman

Formatted: None, Font: Times New Roman

Formatted: None, Font: Times New Roman

Formatted: None, Font: Times New Roman

Deleted: (

Deleted: ,

Formatted: None, Font: Times New Roman

of the tracked plume (forward or backward) to this background. Technically, the SRM in FLEXPART is calculated for a receptor with a certain mean mixing ratio (χ) and an emitting source ($q_{i,n}$) in a certain discretization of the space (index i) and time (index n), as:

$$\frac{\chi}{q_{i,n}} = \frac{1}{J} \sum_{j=1}^J \Delta t_{i,j,n} \frac{p_{j,n}}{\rho_{i,n}} \quad (12)$$

where J is the total number of backward trajectories (particles index j) originating from the position of the receptor χ and ending at a certain discretized time (index n), in certain discretized space position (index i) for a time interval $\Delta t_{i,j,n}$, and where the air density is $\rho_{i,n}$. The further function $p_{j,n}$ ($p_{j,n} \leq 1$) represents the relative (to the initial receptor state) decay of the mass value in the particle in its travel from the receptor to the discretized space time interval (j, n) due to any linear decay process (e.g. deposition, linear chemical decay) for a perfectly conserved scalar $p_{j,n} = 1$. So, for linear decaying species a direct SRM can be calculated explicitly among all relevant receptor points and all positions in space and time. The existence of the SRM (H), linking directly mixing ratios at the receptor points with emissions, is the pre-requisite to apply simple inversion algorithms such as the one we use in the present study.

Inversion of observation to obtain emission for non-linear chemically reactive species entails the need to run a chemistry transport model (CTM) forward (and its adjoint backward) in time from time t_0 to time t_1 , evolving the full state of the atmosphere in relation to the emissions and boundary conditions. Subsequently, a cost function is evaluated by an iterative descent gradient method that implies running the adjoint of the forward model (Fortems-Cheiney et al., 2021). Note that an iterative algorithm means that the forward and adjoint models run several times in sequence until the estimated minimum of the cost function is reached.

To overcome these complexities, we examine the linearities of our method and show that FLEXPART simulates ammonia efficiently, we evaluate modelled ammonia against ground-based measurements of ammonia from the EMEP network (<https://emep.int/mscw/>) in Europe, EANET (East Asia acid deposition NETWORK) in Southeastern Asia (<https://www.eanet.asia/>) and AMoN (Ammonia Monitoring Network in the US, AMoN-US; National Air Pollution Surveillance Program (NAPS) sites in Canada) in North America (<http://nadp.slh.wisc.edu/data/AMoN/>). The SRMs for ammonia calculated with the backward mode express the emission sensitivity (in seconds), which yields a modelled concentration in the receptor point (station) when coupled with gridded emissions (in $\text{kg m}^{-2} \text{s}^{-1}$) at the lowest model level (100 m). Here, we used the ECLIPSEv5, GFED4 and GEIA, (EGG) emissions

Formatted: None, Font: Cambria

Formatted: None, Font: Times New Roman

Formatted

... [1]

Formatted

... [2]

Formatted: None, Font: Times New Roman

Deleted: 1

Formatted

... [3]

Formatted: None, Font: Times New Roman

Formatted: Centred

Field Code Changed

Formatted

... [4]

Formatted

... [5]

Formatted

... [6]

Formatted

... [7]

Formatted

... [8]

Formatted: None, Font: Times New Roman

Formatted

... [9]

Formatted

... [10]

Formatted

... [11]

Formatted

... [12]

Formatted: None, Font: Times New Roman

Formatted

... [13]

Formatted: None, Font: Times New Roman

Formatted: None, Font: Times New Roman

Formatted

... [14]

Formatted

... [15]

Formatted: None, Font: Times New Roman

Formatted: Justified, Indent: First line: 1 cm, Line spacing: 1.5 lines

(Bouwman et al., 1997; Giglio et al., 2013; Klimont et al., 2017) to get concentrations. To check the consistency of the proxy used in the SRMs of ammonia, we also simulated surface concentrations of ammonia with FLEXPART in forward mode using the same emissions. We have chosen two random ground-based stations from each of the three measuring networks (EMEP, EANET, AMoN) to compare modelled concentrations. For consistency, we also plot the resulting surface concentrations from the LMDz-OR-INCA model (Supplementary Figure S 9).

Modelled concentrations (forward and backward FLEXPART and the CTM LMDz-OR-INCA) at each station have been averaged to the temporal resolution of the observations. Supplementary Figure S 10 shows Taylor diagrams of the comparison between FLEXPART simulated concentration in forward and backward mode. Plotting backward versus forward results is a common procedure to infer whether a Lagrangian model produces reasonable results (Eckhardt et al., 2017; Pisso et al., 2019). In general, the forward and backward simulations show very good agreement for the depicted receptor points. For example, ammonia concentration at stations AL99, CA83, and VNA001 (Supplementary Figure S 9) are simulated similarly, and the mean concentrations are almost identical in the forward and backward modes. However, during some episodes there can be notable differences (e.g., at DE0002R) as seen before (Eckhardt et al., 2017). The Taylor diagram for the respective comparison (Supplementary Figure S 10) show high Pearson's correlation coefficients (>0.7), low standard deviations ($<1 \mu\text{g N m}^{-3}$) and root means square errors (RMSEs $<0.7 \mu\text{g N m}^{-3}$).

5 Conclusions

Today, a large debate takes place about ammonia abatement strategies for Europe, but also for Southeastern Asia, in an effort to reduce secondary formation and, thus, mitigate climate crisis (van Vuuren et al., 2015). These strategies include (a) low nitrogen feed by reducing ammonia emissions at many stages of manure management, from excretion in housing, through storage of manure to application on land, also having positive effects on animal health and indoor climate (Montalvo et al., 2015); (b) low emission livestock housing, which focuses on reducing the surface and time manure is exposed to air by adopting rules and regulations regarding new livestock houses (Poteko et al., 2019); (c) air purification by adopting technologies to clean exhaust air from livestock buildings (Cao et al., 2023) and others. Here we used satellite observations from CrIS and a novel inverse modelling algorithm to study the spatial variability and seasonality of ammonia emissions over Europe. We then

Formatted: None, Font: Times New Roman

Formatted: Font: (Default) Times New Roman, Font colour: Auto

Formatted: None, Font: Times New Roman

Formatted: None

Formatted: Font: (Default) Times New Roman, Font colour: Auto

Formatted: Font: (Default) Times New Roman, Font colour: Auto

Formatted: Font: (Default) Times New Roman, Font colour: Auto

Formatted: None, Font: Times New Roman

778 evaluated the overall impact of such strategies on the emissions of ammonia for the period
779 2013–2020. The main key messages can be summarized below:

- 780 • The highest emissions over the 2013–2020 study period occur in North Europe (Belgium,
781 the Netherlands and northwestern Germany). At a regional scale, peaks are seen in Western
782 Europe (Poland, South Romania and Croatia) due to industrial activities, in Spain (Ebro
783 Valley, Aragon, Catalonia) due to agricultural activities and farming, in Belgium and The
784 Netherlands due to livestock activity (dairy cow, beef cattle, pig and chicken farming).
- 785 • Ammonia emissions are low in winter (average: 286 Gg) and peak in summer (average:
786 563 Gg), due to temperature dependent volatilization of ammonia, while a notable peak
787 attributed to fertilization can be seen in early spring during some years.
- 788 • Over the 2013–2020 period, European emissions of ammonia decreased from 5431 Gg in
789 2013 to 3994 Gg in 2020 or about -26%. Hence, the restrictions adopted by the European
790 Union members were effective in reducing secondary PM formation.
- 791 • A slight emission increase of +4.4% in 2015 appears for several European Union Member
792 States (Germany, Spain, France, and the United Kingdom) who exceeded the respective
793 ammonia emission targets. Part of the 2020 ammonia decrease might be attributable to the
794 COVID-19 pandemic restrictions.
- 795 • The largest decreases in ammonia emissions were observed in Central and Eastern Europe
796 (-38%, 2190 Gg in 2013 to 1495 Gg in 2020) and in Western Europe (-37%, 2041 Gg in
797 2013 to 1421 Gg in 2020). Smaller decreases were calculated in Northern Europe (-17%,
798 398 Gg in 2013 to 333 Gg in 2020) and, Southern Europe (-7.6%, from 803 Gg in 2013 to
799 to 743 Gg in 2020).
- 800 • The maximum calculated absolute uncertainty of Gaussian posterior model was 23.3 ng m⁻²
801 s⁻¹, or about 39% (relative value) and calculated maximum based ensemble of prior
802 emissions was 60.2 ng m⁻² s⁻¹, or about 101% following the spatial distribution of the
803 posterior emissions.
- 804 • Comparison of the concentrations calculated with prior and posterior ammonia emissions
805 against independent (not used in the inversion algorithm) observations showed improved
806 correlation coefficients and low nRMSEs and standard deviations. Looking at timeseries
807 of six randomly selected stations in Europe, we also found that posterior surface
808 concentrations of ammonia were in accordance with the ground-based measurement, also
809 following the observed seasonal trends.

Deleted: Here, we examine the impact of such strategies adopted by several European countries on the emissions of ammonia inferred using satellite observations from CrIS and a novel inverse modelling algorithm. We examine and assess the changes on ammonia emissions for the period 2013–2020....

Deleted: during

Deleted: applications

Deleted: emissions

Deleted: 25

Deleted: 42

- Our results agree very well with those from Luo et al. (2022) (decreasing trend: -1.44 versus -1.27 Tg, annual European emissions: 4.63 versus 5.05 Tg) and those from Cao et al. (2022) following their methodology (their posterior_{bi} estimate for EU25 and year 2016 was 2850 Gg N y⁻¹, while we calculate 2712 Gg N y⁻¹).
- The relatively low posterior uncertainty and improved statistics in the validation of the posterior surface concentrations denote the robustness of the posterior emissions of ammonia calculated with satellite measurements and our adapted inverse framework.

Data availability. The data generated for the present paper can be downloaded from ZENODO (<https://doi.org/10.5281/zenodo.7646462>). FLEXPARTv10.4 is open access and can be downloaded from <https://www.flexpart.eu/downloads>, while use of ERA5 data is free of charge, worldwide, non-exclusive, royalty-free and perpetual. The inversion algorithm LS-APC is open access from https://www.utia.cas.cz/linear_inversion_methods. CrIS ammonia can be obtained by request to Dr. M. Shephard (Mark.Shephard@ec.gc.ca). EMEP measurements are open in <https://ebas.nilu.no>. FLEXPART SRMs for 2013–2020 can be obtained from the corresponding author upon request.

Competing interests. The authors declare no competing interests.

Acknowledgements. This study was supported by the Research Council of Norway (project ID: 275407, COMBAT – Quantification of Global Ammonia Sources constrained by a Bayesian Inversion Technique). We kindly acknowledge Dr. M. Shephard for providing CrIS ammonia. This work was granted access to the HPC resources of TGCC under the allocation A0130102201 made by GENCI (Grand Equipement National de Calcul Intensif). [Ondřej Tichý](#) was supported by the Czech Science Foundation, grant no. GA20-27939S.

Author contributions. O.T. adapted the inversion algorithm, performed the calculations, analyses and wrote the paper. S.E. adapted FLEXPARTv10.4 to model ammonia chemical loss. Y.B. and D.H. set up the CTM model and performed the simulation, the output of which was used as input in FLEXPART. N.E. performed the FLEXPART simulations, contributed to analyses, wrote and coordinated the paper. All authors contributed to the final version of the manuscript.

References

- Abbatt, J. P. D., Benz, S., Cziczo, D. J., Kanji, Z., Lohmann, U. and Mohler, O.: Solid Ammonium Sulfate Aerosols as Ice Nuclei: A Pathway for Cirrus Cloud Formation, *Science* (80-.), 313(September), 1770–1773, 2006.
- Beaudor, M., Vuichard, N., Lathière, J., Evangeliou, N., Damme, M. Van, Clarisse, L. and Hauglustaine, D.: Global agricultural ammonia emissions simulated with the ORCHIDEE land surface model, *Geosci. Model Dev.*, 16, 1053–1081 [online] Available from: <https://doi.org/10.5194/egusphere-2022-626>, 2023.
- Behera, S. N., Sharma, M., Aneja, V. P. and Balasubramanian, R.: Ammonia in the atmosphere: A review on emission sources, atmospheric chemistry and deposition on terrestrial bodies, *Environ. Sci. Pollut. Res.*, 20(11), 8092–8131, doi:10.1007/s11356-013-2051-9, 2013.
- Bouwman, A. F., Lee, D. S., Asman, W. A. H., Dentener, F. J., Van Der Hoek, K. W. and Olivier, J. G. J.: A global high-resolution emission inventory for ammonia, *Global Biogeochem. Cycles*, 11(4), 561–587, doi:10.1029/97GB02266, 1997.
- Cao, H., Henze, D. K., Shephard, M. W., Dammers, E., Cady-Pereira, K., Alvarado, M., Lonsdale, C., Luo, G., Yu, F., Zhu, L., Danielson, C. G. and Edgerton, E. S.: Inverse modeling of NH₃ sources using CrIS remote sensing measurements, *Environ. Res. Lett.*, 15, 104082, doi:10.1088/1748-9326/abb5cc, 2020.
- Cao, H., Henze, D. K., Zhu, L., Shephard, M. W., Cady-Pereira, K., Dammers, E., Sitwell, M., Heath, N., Lonsdale, C., Bash, J. O., Miyazaki, K., Flechard, C., Fauvel, Y., Kruit, R. W., Feigenspan, S., Brümmer, C., Schrader, F., Twigg, M. M., Leeson, S., Tang, Y. S., Stephens, A. C. M., Braban, C., Vincent, K., Meier, M., Seitter, E., Geels, C., Ellermann, T., Sanocka, A. and Capps, S. L.: 4D-Var Inversion of European NH₃ Emissions Using CrIS NH₃ Measurements and GEOS-Chem Adjoint With Bi-Directional and Uni-Directional Flux Schemes, *J. Geophys. Res. Atmos.*, 127(9), 1–25, doi:10.1029/2021JD035687, 2022.
- Cao, T., Zheng, Y., Dong, H., Wang, S., Zhang, Y. and Cong, Q.: A new air cleaning technology to synergistically reduce odor and bioaerosol emissions from livestock houses, *Agric. Ecosyst. Environ.*, 342(October 2022), 108221, doi:10.1016/j.agee.2022.108221, 2023.
- Cassiani, M., Stohl, A. and Brioude, J.: Lagrangian Stochastic Modelling of Dispersion in the Convective Boundary Layer with Skewed Turbulence Conditions and a Vertical Density Gradient: Formulation and Implementation in the FLEXPART Model, *Boundary-Layer Meteorol.*, 154(3), 367–390, doi:10.1007/s10546-014-9976-5, 2014.
- Clarisse, L., Van Damme, M., Clerbaux, C. and Coheur, P. F.: Tracking down global NH₃ point sources with wind-adjusted superresolution, *Atmos. Meas. Tech.*, 12(10), 5457–5473, doi:10.5194/amt-12-5457-2019, 2019.
- Crippa, M., Solazzo, E., Huang, G., Guizzardi, D., Koffi, E., Muntean, M., Schieberle, C., Friedrich, R. and Janssens-Maenhout, G.: High resolution temporal profiles in the Emissions Database for Global Atmospheric Research, *Sci. Data*, 7(1), 1–17, doi:10.1038/s41597-020-0462-2, 2020.
- D'Errico, J.: Inpaint_nans, [online] Available from: https://www.mathworks.com/matlabcentral/fileexchange/4551-inpaint_nans, 2023.
- Van Damme, M., Clarisse, L., Dammers, E., Liu, X., Nowak, J. B., Clerbaux, C., Flechard, C. R., Galy-Lacaux, C., Xu, W., Neuman, J. A., Tang, Y. S., Sutton, M. A., Erisman, J. W. and Coheur, P. F.: Towards validation of ammonia (NH₃) measurements from the IASI satellite, *Atmos. Meas. Tech.*, 8(3), 1575–1591, doi:10.5194/amt-8-1575-2015, 2015.

905 Van Damme, M., Whitburn, S., Clarisse, L., Clerbaux, C., Hurtmans, D. and Coheur,
 906 P.: Version 2 of the IASI NH 3 neural network retrieval algorithm : near-real-time and
 907 reanalysed datasets, *Atmos. Meas. Tech.*, 10, 4905–4914, 2017.
 908 Van Damme, M., Clarisse, L., Whitburn, S., Hadji-Lazaro, J., Hurtmans, D., Clerbaux,
 909 C. and Coheur, P. F.: Industrial and agricultural ammonia point sources exposed,
 910 *Nature*, 564(7734), 99–103, doi:10.1038/s41586-018-0747-1, 2018.
 911 Van Damme, M., Clarisse, L., Stavrakou, T., Wichink Kruit, R., Sellekaerts, L., Viatte,
 912 C., Clerbaux, C. and Coheur, P. F.: On the weekly cycle of atmospheric ammonia
 913 over European agricultural hotspots, *Sci. Rep.*, 12(1), 1–9, doi:10.1038/s41598-022-
 914 15836-w, 2022.
 915 Dammers, E., Palm, M., Van Damme, M., Vigouroux, C., Smale, D., Conway, S.,
 916 Toon, G. C., Jones, N., Nussbaumer, E., Warneke, T., Petri, C., Clarisse, L.,
 917 Clerbaux, C., Hermans, C., Lutsch, E., Strong, K., Hannigan, J. W., Nakajima, H.,
 918 Morino, I., Herrera, B., Stremme, W., Grutter, M., Schaap, M., Kruit, R. J. W., Notholt,
 919 J., Coheur, P. F. and Erisman, J. W.: An evaluation of IASI-NH 3 with ground-based
 920 Fourier transform infrared spectroscopy measurements, *Atmos. Chem. Phys.*,
 921 16(16), 10351–10368, doi:10.5194/acp-16-10351-2016, 2016.
 922 Dammers, E., Shephard, M. W., Palm, M., Cady-pereira, K., Capps, S., Lutsch, E.,
 923 Strong, K., Hannigan, J. W., Ortega, I., Toon, G. C., Stremme, W. and Grutter, M.:
 924 Validation of the CrIS fast physical NH 3 retrieval with ground-based FTIR, *Atmos.*
 925 *Meas. Tech.*, 87, 2645–2667, 2017.
 926 Dammers, E., McLinden, C. A., Griffin, D., Shephard, M. W., Van Der Graaf, S.,
 927 Lutsch, E., Schaap, M., Gainairu-Matz, Y., Fioletov, V., Van Damme, M., Whitburn,
 928 S., Clarisse, L., Cady-Pereira, K., Clerbaux, C., Francois Coheur, P. and Erisman, J.
 929 W.: NH₃ emissions from large point sources derived from CrIS and IASI satellite
 930 observations, *Atmos. Chem. Phys.*, 19(19), 12261–12293, doi:10.5194/acp-19-
 931 12261-2019, 2019.
 932 Dee, D. P., Uppala, S. M., Simmons, A. J., Berrisford, P., Poli, P., Kobayashi, S.,
 933 Andrae, U., Balmaseda, M. A., Balsamo, G., Bauer, P., Bechtold, P., Beljaars, A. C.
 934 M., van de Berg, L., Bidlot, J., Bormann, N., Delsol, C., Dragani, R., Fuentes, M.,
 935 Geer, A. J., Haimberger, L., Healy, S. B., Hersbach, H., H²lm, E. V., Isaksen, I.,
 936 K²llberg, P., K²hler, M., Matricardi, M., McNally, A. P., Monge-Sanz, B. M.,
 937 Morcrette, J. J., Park, B. K., Peubey, C., de Rosnay, P., Tavolato, C., Th²paut, J. N.
 938 and Vitart, F.: The ERA-Interim reanalysis: Configuration and performance of the
 939 data assimilation system, *Q. J. R. Meteorol. Soc.*, 137(656), 553–597,
 940 doi:10.1002/qj.828, 2011.
 941 Eckhardt, S., Cassiani, M., Evangeliou, N., Sollum, E., Pisso, I. and Stohl, A.:
 942 Source-receptor matrix calculation for deposited mass with the Lagrangian particle
 943 dispersion model FLEXPART v10.2 in backward mode, *Geosci. Model Dev.*, 10,
 944 4605–4618, doi:10.5194/gmd-10-4605-2017, 2017.
 945 EEA: European Union emission inventory report 1990 –2015 under the UNECE
 946 Convention on Long-range Transboundary Air Pollution. [online] Available from:
 947 <https://www.eea.europa.eu/publications/annual-eu-emissions-inventory-report>, 2017.
 948 Emanuel, K. A.: A Scheme for Representing Cumulus Convection in Large-Scale
 949 Models, *J. Atmos. Sci.*, 48(21), 2313–2329, doi:10.1175/1520-
 950 0469(1991)048<2313:ASFRCC>2.0.CO;2, 1991.
 951 Erisman, J. W., Bleeker, A., Galloway, J. and Sutton, M. S.: Reduced nitrogen in
 952 ecology and the environment, *Environ. Pollut.*, 150(1), 140–149,
 953 doi:10.1016/j.envpol.2007.06.033, 2007.
 954 Evangeliou, N., Balkanski, Y., Eckhardt, S., Cozic, A., Van Damme, M., Coheur, P.-

955 F., Clarisse, L., Shephard, M., Cady-Pereira, K. and Hauglustaine, D.: 10-Year
 956 Satellite-Constrained Fluxes of Ammonia Improve Performance of Chemistry
 957 Transport Models, *Atmos. Chem. Phys.*, 21, 4431–4451, doi:10.5194/acp-21-4431-
 958 2021, 2021.
 959 Fang, S., Dong, X., Zhuang, S., Tian, Z., Zhao, Y., Liu, Y., Liu, Y. and Sheng, L.:
 960 Inversion of ¹³⁷Cs emissions following the Fukushima accident with adaptive release
 961 recovery for temporal absences of observations, *Environ. Pollut.*, 317(September
 962 2022), 120814, doi:10.1016/j.envpol.2022.120814, 2023.
 963 Forster, C., Stohl, A. and Seibert, P.: Parameterization of convective transport in a
 964 Lagrangian particle dispersion model and its evaluation, *J. Appl. Meteorol. Climatol.*,
 965 46(4), 403–422, doi:10.1175/JAM2470.1, 2007.
 966 Fortems-Cheiney, A., Pison, I., Broquet, G., Dufour, G., Berchet, A., Potier, E.,
 967 Coman, A., Siour, G. and Costantino, L.: Variational regional inverse modeling of
 968 reactive species emissions with PYVAR-CHIMERE-v2019, *Geosci. Model Dev.*,
 969 14(5), 2939–2957, doi:10.5194/gmd-14-2939-2021, 2021.
 970 Fowler, D., Müller, J. B. A., Smith, R. I., Dragosits, U., Skiba, U., Sutton, M. A. and
 971 Brimblecombe, P.: A CHRONOLOGY OF NITROGEN DEPOSITION IN THE UK,
 972 *Water, Air, Soil Pollut. Focus*, 4, 9–23, 2004.
 973 Galloway, J. N., Aber, J. D., Erisman, J. A. N. W., Seitzinger, S. P., Howarth, R. W.,
 974 Cowling, E. B. and Cosby, B. J.: The Nitrogen Cascade, *Bioscience*, 53(4), 341–356,
 975 doi:10.1641/0006-3568(2003)053[0341:TNC]2.0.CO;2, 2003.
 976 Ge, X., Schaap, M., Kranenburg, R., Segers, A., Jan Reinds, G., Kros, H. and De
 977 Vries, W.: Modeling atmospheric ammonia using agricultural emissions with
 978 improved spatial variability and temporal dynamics, *Atmos. Chem. Phys.*, 20(24),
 979 16055–16087, doi:10.5194/acp-20-16055-2020, 2020.
 980 Giannakis, E., Kushta, J., Bruggeman, A. and Lelieveld, J.: Costs and benefits of
 981 agricultural ammonia emission abatement options for compliance with European air
 982 quality regulations, *Environ. Sci. Eur.*, 31(1), doi:10.1186/s12302-019-0275-0, 2019.
 983 Giglio, L., Randerson, J. T. and van der Werf, G. R.: Analysis of daily, monthly, and
 984 annual burned area using the fourth-generation global fire emissions database
 985 (GFED4), *J. Geophys. Res. Biogeosciences*, 118, 317–328, doi:10.1002/jgrg.20042,
 986 2013, 2013.
 987 Gilbert, M., Nicolas, G., Cinardi, G., Van Boeckel, T. P., Vanwambeke, S. O., Wint,
 988 G. R. W. and Robinson, T. P.: Global distribution data for cattle, buffaloes, horses,
 989 sheep, goats, pigs, chickens and ducks in 2010, *Sci. Data*, 5, 1–11,
 990 doi:10.1038/sdata.2018.227, 2018.
 991 Hauglustaine, D. A., Hourdin, F., Jourdain, L., Filiberti, M.-A., Walters, S., Lamarque,
 992 J.-F. and Holland, E. A.: Interactive chemistry in the Laboratoire de Meteorologie
 993 Dynamique general circulation model: Description and background tropospheric
 994 chemistry evaluation, *J. Geophys. Res.*, 109(D04314), doi:10.1029/2003JD003957,
 995 2004.
 996 Hauglustaine, D. A., Balkanski, Y. and Schulz, M.: A global model simulation of
 997 present and future nitrate aerosols and their direct radiative forcing of climate, *Atmos.*
 998 *Chem. Phys.*, 14(20), 11031–11063, doi:10.5194/acp-14-11031-2014, 2014.
 999 Henze, D. K., Shindell, D. T., Akhtar, F., Spurr, R. J. D., Pinder, R. W., Loughlin, D.,
 1000 Kopacz, M., Singh, K. and Shim, C.: Spatially Refined Aerosol Direct Radiative
 1001 Forcing Efficiencies, *Environ. Sci. Technol.*, 46, 9511–9518, doi:10.1021/es301993s,
 1002 2012.
 1003 Hersbach, H., Bell, B., Berrisford, P., Hirahara, S., Horányi, A., Muñoz-Sabater, J.,
 1004 Nicolas, J., Peubey, C., Radu, R., Schepers, D., Simmons, A., Soci, C., Abdalla, S.,

1005 Abellan, X., Balsamo, G., Bechtold, P., Biavati, G., Bidlot, J., Bonavita, M., De
 1006 Chiara, G., Dahlgren, P., Dee, D., Diamantakis, M., Dragani, R., Flemming, J.,
 1007 Forbes, R., Fuentes, M., Geer, A., Haimberger, L., Healy, S., Hogan, R. J., Hólm, E.,
 1008 Janisková, M., Keeley, S., Laloyaux, P., Lopez, P., Lupu, C., Radnoti, G., de Rosnay,
 1009 P., Rozum, I., Vamborg, F., Villaume, S. and Thépaut, J. N.: The ERA5 global
 1010 reanalysis, *Q. J. R. Meteorol. Soc.*, 146(730), 1999–2049, doi:10.1002/qj.3803, 2020.
 1011 Hourdin, F. and Armengaud, A.: The Use of Finite-Volume Methods for Atmospheric
 1012 Advection of Trace Species. Part I: Test of Various Formulations in a General
 1013 Circulation Model, *Mon. Weather Rev.*, 127(5), 822–837, doi:10.1175/1520-
 1014 0493(1999)127<0822:TUOFVM>2.0.CO;2, 1999.
 1015 Hourdin, F., Musat, I., Bony, S., Braconnot, P., Codron, F., Dufresne, J. L., Fairhead,
 1016 L., Filiberti, M. A., Friedlingstein, P., Grandpeix, J. Y., Krinner, G., LeVan, P., Li, Z. X.
 1017 and Lott, F.: The LMDZ4 general circulation model: Climate performance and
 1018 sensitivity to parametrized physics with emphasis on tropical convection, *Clim. Dyn.*,
 1019 27(7–8), 787–813, doi:10.1007/s00382-006-0158-0, 2006.
 1020 Kharol, S. K., Shephard, M. W., McLinden, C. A., Zhang, L., Sioris, C. E., O'Brien, J.
 1021 M., Vet, R., Cady-Pereira, K. E., Hare, E., Siemons, J. and Krotkov, N. A.: Dry
 1022 Deposition of Reactive Nitrogen From Satellite Observations of Ammonia and
 1023 Nitrogen Dioxide Over North America, *Geophys. Res. Lett.*, 45(2), 1157–1166,
 1024 doi:10.1002/2017GL075832, 2018.
 1025 Klimont, Z.: personal communication, 2022.
 1026 Klimont, Z., Kupiainen, K., Heyes, C., Purohit, P., Cofala, J., Rafaj, P., Borken-
 1027 Kleefeld, J. and Schöpp, W.: Global anthropogenic emissions of particulate matter
 1028 including black carbon, *Atmos. Chem. Phys.*, 17, 8681–8723, doi:10.5194/acp-17- 50
 1029 8681-2017, 2017.
 1030 Krupa, S. V.: Effects of atmospheric ammonia (NH₃) on terrestrial vegetation: A
 1031 review, *Environ. Pollut.*, 124(2), 179–221, doi:10.1016/S0269-7491(02)00434-7,
 1032 2003.
 1033 Kuhn, T.: The revision of the German Fertiliser Ordinance in 2017, *Agric. Resour.*
 1034 *Econ.*, 2(Discussion Paper), 1–22, 2017.
 1035 Lassaletta, L., Romero, E., Billen, G., Garnier, J., García-Gómez, H. and Rovira, J.
 1036 V.: Spatialized N budgets in a large agricultural Mediterranean watershed: High
 1037 loading and low transfer, *Biogeosciences*, 9(1), 57–70, doi:10.5194/bg-9-57-2012,
 1038 2012.
 1039 Lecina, S., Isidoro, D., Playán, E. and Aragüés, R.: Irrigation modernization in Spain:
 1040 Effects on water quantity and quality-a conceptual approach, *Int. J. Water Resour.*
 1041 *Dev.*, 26(2), 265–282, doi:10.1080/07900621003655734, 2010.
 1042 Lelieveld, J., Evans, J. S., Fnais, M., Giannadaki, D. and Pozzer, A.: The contribution
 1043 of outdoor air pollution sources to premature mortality on a global scale., *Nature*,
 1044 525(7569), 367–71, doi:10.1038/nature15371, 2015.
 1045 Lesschen, J. P., van den Berg, M., Westhoek, H. J., Witzke, H. P. and Oenema, O.:
 1046 Greenhouse gas emission profiles of European livestock sectors, *Anim. Feed Sci.*
 1047 *Technol.*, 166–167, 16–28, doi:10.1016/j.anifeedsci.2011.04.058, 2011.
 1048 Li, C., Martin, R. V., Shephard, M. W., Pereira, K. C., Cooper, M. J., Kaiser, J., Lee,
 1049 C. J., Zhang, L. and Henze, D. K.: Assessing the Iterative Finite Difference Mass
 1050 Balance and 4D - Var Methods to Derive Ammonia Emissions Over North America
 1051 Using Synthetic Observations, *J. Geophys. Res. Atmos.*, 124, 4222–4236,
 1052 doi:10.1029/2018JD030183, 2019.
 1053 Lonati, G. and Cernuschi, S.: Temporal and spatial variability of atmospheric
 1054 ammonia in the Lombardy region (Northern Italy), *Atmos. Pollut. Res.*, 11(12), 2154–

1055 2163, doi:10.1016/j.apr.2020.06.004, 2020.
 1056 Luo, Z., Zhang, Y., Chen, W., Van Damme, M., Coheur, P.-F. and Clarisse, L.:
 1057 Estimating global ammonia (NH₃) emissions based on IASI observations from 2008
 1058 to 2018, *Atmos. Chem. Phys.*, 22(15), 10375–10388, doi:10.5194/acp-22-10375-
 1059 2022, 2022.
 1060 Malm, W. C.: Spatial and monthly trends in speciated fine particle concentration in
 1061 the United States, *J. Geophys. Res.*, 109(D3), D03306, doi:10.1029/2003JD003739,
 1062 2004.
 1063 McDuffie, E., Smith, S., O'Rourke, P., Tibrewal, K., Venkataraman, C., Marais, E.,
 1064 Zheng, B., Crippa, M., Brauer, M. and Martin, R.: A global anthropogenic emission
 1065 inventory of atmospheric pollutants from sector- and fuel-specific sources (1970–
 1066 2017): An application of the Community Emissions Data System (CEDS), *Earth Syst.*
 1067 *Sci. Data Discuss.*, 1–49, doi:10.5194/essd-2020-103, 2020.
 1068 Montalvo, G., Pineiro, C., Herrero, M., Biegeriego, M. and Prins, W.: Ammonia
 1069 Abatement by Animal Housing Techniques BT - Costs of Ammonia Abatement and
 1070 the Climate Co-Benefits, edited by S. Reis, C. Howard, and M. A. Sutton, pp. 53–73,
 1071 Springer Netherlands, Dordrecht., 2015.
 1072 Paulot, F., Jacob, D. J., Pinder, R. W., Bash, J. O., Travis, K. and Henze, D. K.:
 1073 Ammonia emissions in the United States, European Union, and China derived by
 1074 high-resolution inversion of ammonium wet deposition data: Interpretation with a new
 1075 agricultural emissions inventory (MASAGE-NH₃), *J. Geophys. Res. Atmos.*, 119(7),
 1076 4343–4364, doi:10.1002/2013JD021130, 2014.
 1077 Pisso, I., Sollum, E., Grythe, H., Kristiansen, N., Cassiani, M., Eckhardt, S., Arnold,
 1078 D., Morton, D., Thompson, R. L., Groot Zwaaftink, C. D., Evangeliou, N., Sodemann,
 1079 H., Haimberger, L., Henne, S., Brunner, D., Burkhardt, J. F., Fouilloux, A., Brioude, J.,
 1080 Philipp, A., Seibert, P. and Stohl, A.: The Lagrangian particle dispersion model
 1081 FLEXPART version 10.4, *Geosci. Model Dev.*, 12, 4955–4997, doi:10.5194/gmd-12-
 1082 4955-2019, 2019.
 1083 Pope, C. A. and Dockery, D. W.: Health effects of fine particulate air pollution: Lines
 1084 that connect, *J. Air Waste Manag. Assoc.*, 56(6), 709–742,
 1085 doi:10.1080/10473289.2006.10464485, 2006.
 1086 Pope III, C. A., Burnett, R. T., Thun, M. J., Calle, E. E., Krewski, D. and Thurston, G.
 1087 D.: Lung Cancer, Cardiopulmonary Mortality, and Long-term Exposure to Fine
 1088 Particulate Air Pollution, *J. Am. Med. Assoc.*, 287(9), 1132–1141,
 1089 doi:10.1001/jama.287.9.1132, 2002.
 1090 Poteko, J., Zähler, M. and Schrader, S.: Effects of housing system, floor type and
 1091 temperature on ammonia and methane emissions from dairy farming: A meta-
 1092 analysis, *Biosyst. Eng.*, 182, 16–28, doi:10.1016/j.biosystemseng.2019.03.012, 2019.
 1093 Rodgers, C. D.: Inverse methods for atmospheres: Theory and practice., 2000.
 1094 Seibert, P. and Frank, A.: Source-receptor matrix calculation with a Lagrangian
 1095 particle dispersion model in backward mode, *Atmos. Chem. Phys.*, 4(1), 51–63,
 1096 doi:10.5194/acp-4-51-2004, 2004.
 1097 Seinfeld, J. H. and Pandis, S. N.: Atmospheric Chemistry and Physics. From Air
 1098 Pollution to Climate Change, 2nd ed., John Wiley & Sons, NY., 2000.
 1099 Shephard, M. W. and Cady-Pereira, K. E.: Cross-track Infrared Sounder (CrIS)
 1100 satellite observations of tropospheric ammonia, *Atmos. Meas. Tech.*, 8(3), 1323–
 1101 1336, doi:10.5194/amt-8-1323-2015, 2015.
 1102 Shephard, M. W., McLinden, C. A., Cady-Pereira, K. E., Luo, M., Moussa, S. G.,
 1103 Leithead, A., Liggio, J., Staebler, R. M., Akingunola, A., Makar, P., Lehr, P., Zhang,
 1104 J., Henze, D. K., Millet, D. B., Bash, J. O., Zhu, L., Wells, K. C., Capps, S. L.,

1105 Chaliyakunnel, S., Gordon, M., Hayden, K., Brook, J. R., Wolde, M. and Li, S. M.:
 1106 Tropospheric Emission Spectrometer (TES) satellite observations of ammonia,
 1107 methanol, formic acid, and carbon monoxide over the Canadian oil sands: Validation
 1108 and model evaluation, *Atmos. Meas. Tech.*, 8(12), 5189–5211, doi:10.5194/amt-8-
 1109 5189-2015, 2015.
 1110 Shephard, M. W., Dammers, E., E. Cady-Pereira, K., K. Kharol, S., Thompson, J.,
 1111 Gainariu-Matz, Y., Zhang, J., A. McLinden, C., Kovachik, A., Moran, M., Bittman, S.,
 1112 E. Sioris, C., Griffin, D., J. Alvarado, M., Lonsdale, C., Savic-Jovicic, V. and Zheng,
 1113 Q.: Ammonia measurements from space with the Cross-track Infrared Sounder:
 1114 Characteristics and applications, *Atmos. Chem. Phys.*, 20(4), 2277–2302,
 1115 doi:10.5194/acp-20-2277-2020, 2020.
 1116 Sigurdarson, J. J., Svane, S. and Karring, H.: The molecular processes of urea
 1117 hydrolysis in relation to ammonia emissions from agriculture, *Rev. Environ. Sci.*
 1118 *Biotechnol.*, 17(2), 241–258, doi:10.1007/s11157-018-9466-1, 2018.
 1119 Sitwell, M. and Shephard, M.: An Ensemble-Variational Inversion System for the
 1120 Estimation of Ammonia Emissions using CrIS Satellite Ammonia Retrievals, , (x),
 1121 2021.
 1122 Sitwell, M., Shephard, M. W., Rochon, Y., Cady-Pereira, K. and Dammers, E.: An
 1123 ensemble-variational inversion system for the estimation of ammonia emissions
 1124 using CrIS satellite ammonia retrievals, *Atmos. Chem. Phys.*, 22(10), 6595–6624,
 1125 doi:10.5194/acp-22-6595-2022, 2022.
 1126 Someya, Y., Imasu, R., Shiomi, K. and Saitoh, N.: Atmospheric ammonia retrieval
 1127 from the TANSO-FTS / GOSAT thermal infrared sounder, *Atmos. Meas. Tech.*, 13,
 1128 309–321, 2020.
 1129 Stevens, C. J., Dupr, C., Dorland, E., Gaudnik, C., Gowing, D. J. G., Bleeker, A.,
 1130 Diekmann, M., Alard, D., Bobbink, R., Fowler, D., Corcket, E., Mountford, J. O.,
 1131 Vandvik, V., Aarrestad, P. A., Muller, S. and Dise, N. B.: Nitrogen deposition
 1132 threatens species richness of grasslands across Europe, *Environ. Pollut.*, 158(9),
 1133 2940–2945, doi:10.1016/j.envpol.2010.06.006, 2010.
 1134 Stohl, A., Forster, C., Frank, A., Seibert, P. and Wotawa, G.: Technical note: The
 1135 Lagrangian particle dispersion model FLEXPART version 6.2, *Atmos. Chem. Phys.*,
 1136 5(9), 2461–2474, doi:10.5194/acp-5-2461-2005, 2005.
 1137 Sutton, M. A., Erisman, J. W., Dentener, F. and Möller, D.: Ammonia in the
 1138 environment: From ancient times to the present, *Environ. Pollut.*, 156(3), 583–604,
 1139 doi:10.1016/j.envpol.2008.03.013, 2008.
 1140 Sutton, M. A., Reis, S., Riddick, S. N., Dragosits, U., Nemitz, E., Theobald, M. R.,
 1141 Tang, Y. S., Braban, C. F., Vieno, M., Dore, A. J., Mitchell, R. F., Wanless, S., Daunt,
 1142 F., Fowler, D., Blackall, T. D., Milford, C., Flechard, C. R., Loubet, B., Massad, R.,
 1143 Cellier, P., Personne, E., Coheur, P. F., Clarisse, L., Damme, M. Van, Ngadi, Y.,
 1144 Clerbaux, C., Skjøth, C. A., Geels, C., Hertel, O., Kruit, R. J. W., Pinder, R. W., Bash,
 1145 J. O., Walker, J. T., Simpson, D., Horvath, L., Misselbrook, T. H., Bleeker, A.,
 1146 Dentener, F. and Vries, W. de: Towards a climate-dependent paradigm of ammonia
 1147 emission and deposition, *Philos. Trans. R. Soc. B Biol. Sci.*, 368(1621), 20130166–
 1148 20130166, doi:10.1098/rstb.2013.0166, 2013.
 1149 Tang, Y. S., Flechard, C., Dämmgen, U., Vidic, S., Djuricic, V., Mitosinkova, M.,
 1150 Uggerud, H., Sanz, M., Simmons, I., Dragosits, U., Nemitz, E., Twigg, M., van Dijk,
 1151 N., Fauvel, Y., Sanz-Sanchez, F., Ferm, M., Perrino, C., Catrambone, M., Leaver, D.,
 1152 Braban, C., Cape, J. N., Heal, M. and Sutton, M.: Pan-European rural atmospheric
 1153 monitoring network shows dominance of NH₃ gas and
 1154 NH₄NO₃ aerosol in inorganic pollution

load, *Atmos. Chem. Phys. Discuss.*, 1–61, 2020.

Tichý, O., Šmídl, V., Hofman, R. and Stohl, A.: LS-APC v1.0: A tuning-free method for the linear inverse problem and its application to source-term determination, *Geosci. Model Dev.*, 9(11), 4297–4311, doi:10.5194/gmd-9-4297-2016, 2016.

Tichý, O., Ulrych, L., Šmídl, V., Evangeliou, N. and Stohl, A.: On the tuning of atmospheric inverse methods: Comparisons with the European Tracer Experiment (ETEX) and Chernobyl datasets using the atmospheric transport model FLEXPART, *Geosci. Model Dev.*, 13(12), 5917–5934, doi:10.5194/gmd-13-5917-2020, 2020.

Tichý, O., Otervik, M. S., Eckhardt, S., Balkanski, Y., Hauglustaine, D. and Evangeliou, N.: NH₃ levels over Europe during COVID-19 were modulated by changes in atmospheric chemistry, *npj Clim. Atmos. Sci.*, in review, 1–13, doi:10.21203/rs.3.rs-1930069/v1, 2022.

Torseth, K., Aas, W., Breivik, K., Fjæraa, A. M., Fiebig, M., Hjellbrekke, A. G., Lund Myhre, C., Solberg, S. and Yttri, K. E.: Introduction to the European Monitoring and Evaluation Programme (EMEP) and observed atmospheric composition change during 1972–2009, *Atmos. Chem. Phys.*, 12(12), 5447–5481, doi:10.5194/acp-12-5447-2012, 2012.

Tsimpidi, A. P., Karydis, V. A. and Pandis, S. N.: Response of inorganic fine particulate matter to emission changes of sulfur dioxide and ammonia: The Eastern United States as a case study, *J. Air Waste Manag. Assoc.*, 57(12), 1489–1498, doi:10.3155/1047-3289.57.12.1489, 2007.

Velthof, G. L., van Bruggen, C., Groenestein, C. M., de Haan, B. J., Hoogeveen, M. W. and Huijsmans, J. F. M.: A model for inventory of ammonia emissions from agriculture in the Netherlands, *Atmos. Environ.*, 46, 248–255, doi:10.1016/j.atmosenv.2011.09.075, 2012.

Vira, J., Hess, P., Melkonian, J. and Wieder, W. R.: An improved mechanistic model for ammonia volatilization in Earth system models: Flow of Agricultural Nitrogen version 2 (FANv2), *Geosci. Model Dev.*, 13(9), 4459–4490, doi:10.5194/gmd-13-4459-2020, 2020.

van Vuuren, A. M., Pineiro, C., van der Hoek, K. W. and Oenema, O.: Economics of Low Nitrogen Feeding Strategies BT - Costs of Ammonia Abatement and the Climate Co-Benefits, edited by S. Reis, C. Howard, and M. A. Sutton, pp. 35–51, Springer Netherlands, Dordrecht., 2015.

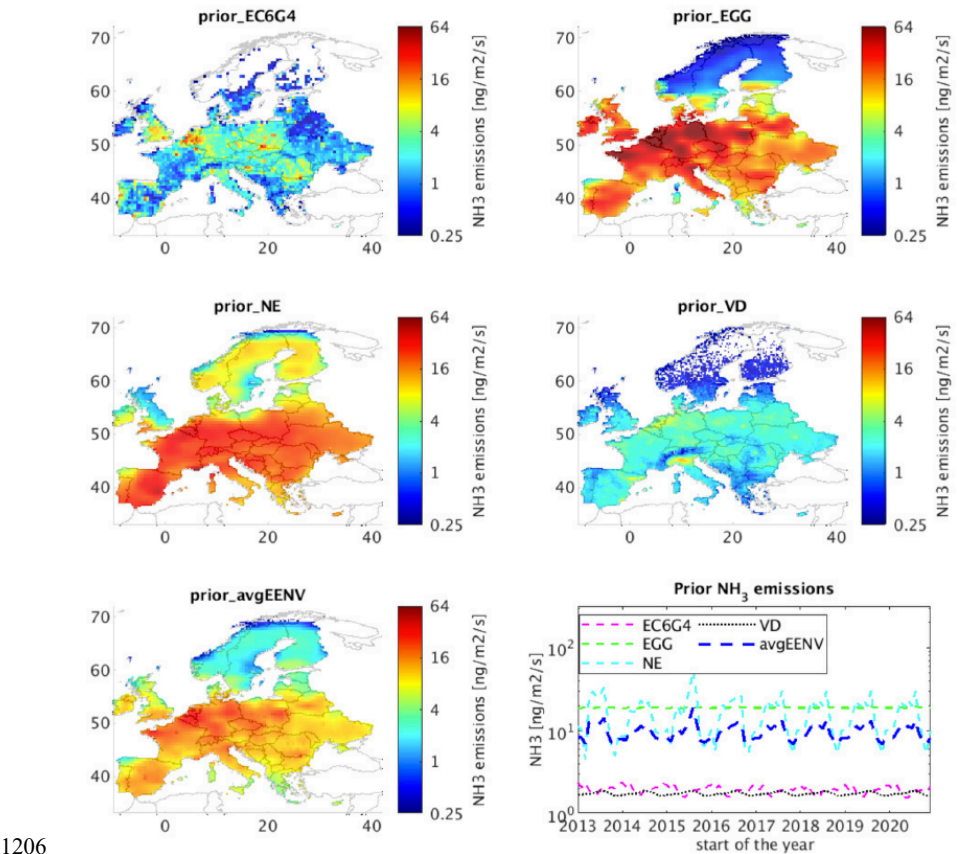
Warner, J. X., Dickerson, R. R., Wei, Z., Strow, L. L., Wang, Y. and Liang, Q.: Increased atmospheric ammonia over the world's major agricultural areas detected from space, *Geophys. Res. Lett.*, 44, 1–10, doi:10.1002/2016GL072305, 2017.

Whitburn, S., Van Damme, M., Clarisse, L., Bauduin, S., Heald, C. L., Hadji-Lazaro, J., Hurtmans, D., Zondlo, M. A., Clerbaux, C. and Coheur, P. F.: A flexible and robust neural network IASI-NH₃ retrieval algorithm, *J. Geophys. Res.*, 121(11), 6581–6599, doi:10.1002/2016JD024828, 2016.

Zavalyov, V., Esplin, M., Scott, D., Esplin, B., Bingham, G., Hoffman, E., Lietzke, C., Predina, J., Frain, R., Suwinski, L., Han, Y., Major, C., Graham, B. and Phillips, L.: Noise performance of the CrIS instrument, , 118, 108–120, doi:10.1002/2013JD020457, 2013.

Zhu, L., Henze, D. K., Cady-Pereira, K. E., Shephard, M. W., Luo, M., Pinder, R. W., Bash, J. O. and Jeong, G. R.: Constraining U.S. ammonia emissions using TES remote sensing observations and the GEOS-Chem adjoint model, *J. Geophys. Res. Atmos.*, 118(8), 3355–3368, doi:10.1002/jgrd.50166, 2013.

1205 **FIGURES & LEGENDS**



1206
1207 **Figure 1.** Four ammonia prior emissions (EC6G4, EGG, NE, VD) are displayed in the first two
1208 rows. The combined prior (avgEENV) is displayed in the bottom left. The temporal variability
1209 of all five prior emissions is given in bottom right.

Deleted: activity

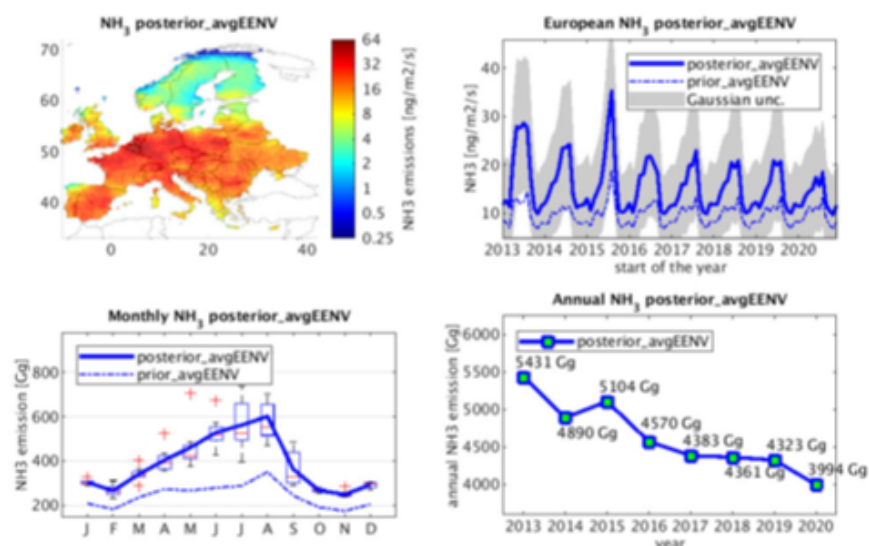
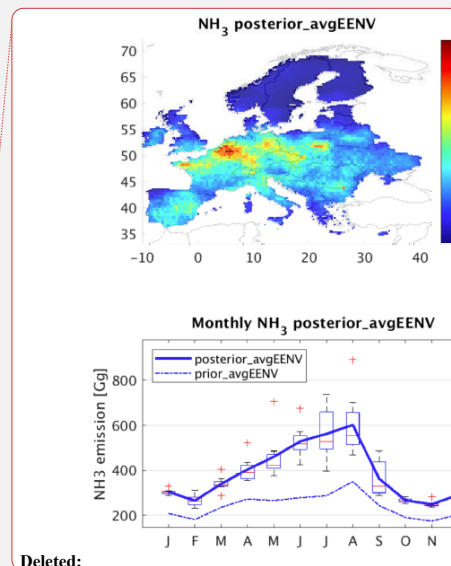


Figure 2. The spatial distribution of posterior ammonia emissions (posterior_EENV, top-left) together with its temporal distribution (top-right). The Gaussian uncertainty of the posterior emissions is also plotted. Monthly average (bottom-left) and annually average (bottom-right) estimates are also plotted. The monthly average posterior emissions over the studied period are accompanied by the box plot where the red line indicates the median, the bottom and top edges of the Boxes indicating the 25th and 75th percentiles, respectively, and the whiskers extend to the most extreme data points not considered as outliers, which are denoted using red crosses. Solid blue lines refer to the posterior ammonia emissions, while dashed ones to the prior emissions (avgEENV).



Deleted:

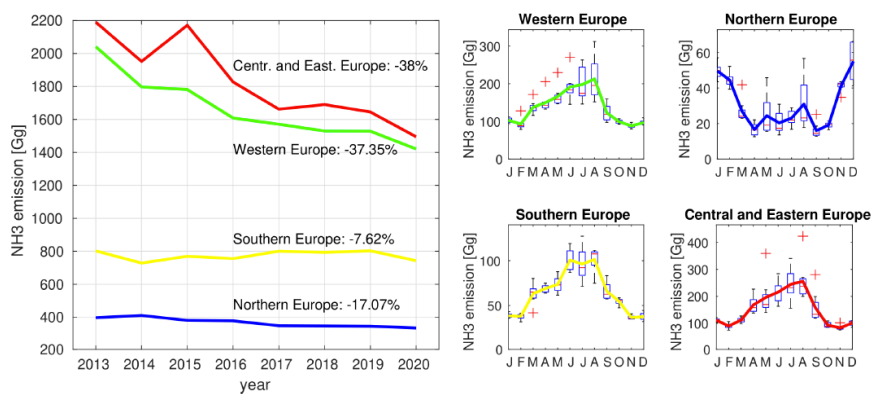


Figure 3. Left: Annual posterior emissions of ammonia in Southern (yellow), Western (green), Northern (blue), and Central and Eastern (red) Europe. Right: Monthly average posterior emissions of ammonia accompanied by box plots, where the red line indicates the median, the bottom and top edges of the box indicate the 25th and 75th percentiles, respectively, and the whiskers extend to the most extreme data points (not considered outliers), which are represented using red crosses.

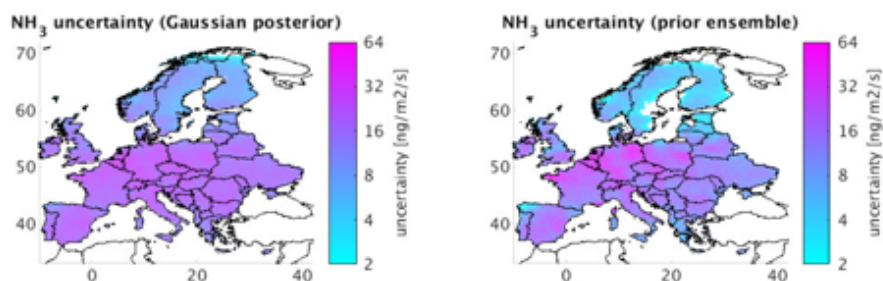
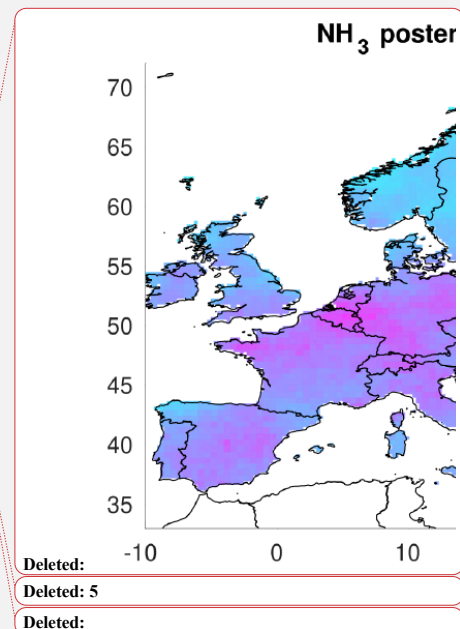
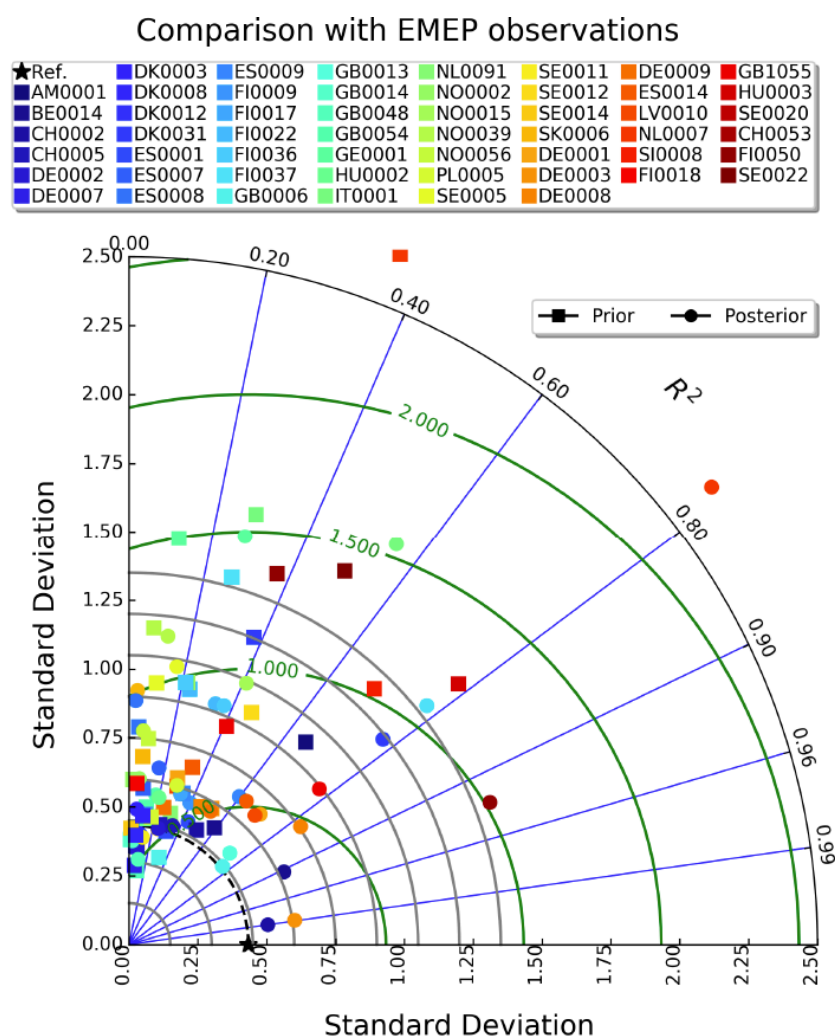


Figure 4. Absolute uncertainty of posterior emissions of ammonia calculated as 2σ (left panel) and from a member ensemble (right panel) comprising posterior emissions calculated with five different priors (Figure 1) averaged for the whole study period 2013–2020.





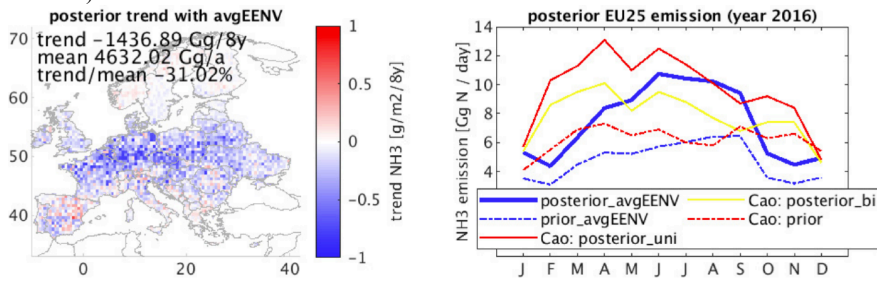
1240

1241 **Figure 5.** Modelled concentrations of ammonia with prior and posterior emissions against
 1242 ground-based observations from 53 EMEP stations for 2013–2020 presented in a Taylor
 1243 diagram. The diagram shows the Pearson's correlation coefficient (gauging similarity in pattern
 1244 between the modelled and observed concentrations) that is related to the azimuthal angle (blue
 1245 contours); the standard deviation of modelled concentrations of ammonia is proportional to the
 1246 radial distance from the origin (black contours) and the centered normalized RMSE of modelled
 1247 concentrations is proportional to the distance from the reference standard deviation (green

Deleted: 6

1249

contours).



1250

1251

Figure 6. Left: spatial distribution of ammonia emission trends computed for the studied period 2013–2020 in the same way as in (Luo et al., 2022), where also trend, mean, and trend/mean are defined/computed in the same way. Right: comparison of ammonia emissions from the EU25 countries for the year 2016 from our posterior calculations (posterior_avgEENV, blue) and results from Cao et al. (2022) (posterior_uni in red and posterior_bi, in yellow).

1256

Deleted: 4

1258
1259